



## ENGINEERING

# Smart patterning for topological pumping of elastic surface waves

Shaoyun Wang<sup>1†</sup>, Zhou Hu<sup>2†</sup>, Qian Wu<sup>1†</sup>, Hui Chen<sup>3</sup>, Emil Prodan<sup>4</sup>, Rui Zhu<sup>2\*</sup>, Guoliang Huang<sup>1\*</sup>

**Topological pumping allows waves to navigate a sample undisturbed by disorders and defects. We demonstrate this phenomenon with elastic surface waves by strategically patterning an elastic surface to create a synthetic dimension. The surface is decorated with arrays of resonating pillars that are connected by spatially slow-varying coupling bridges and support eigenmodes located below the sound cone. We establish a connection between the collective dynamics of the pillars and that of electrons in a magnetic field by developing a tight-binding model and a WKB (Wentzel-Kramers-Brillouin) analysis. This enables us to predict the topological pumping pattern, which we validate through numerical and experimental steering of waves from one edge to the other. Furthermore, we observe the immune nature of the topologically pumped surface waves to disorder and defects. The combination of surface patterning and WKB analysis provides a versatile platform for controlling surface waves and exploring topological matter in higher dimensions.**

Copyright © 2023 The Authors, some rights reserved; exclusive licensee American Association for the Advancement of Science. No claim to original U.S. Government Works. Distributed under a Creative Commons Attribution NonCommercial License 4.0 (CC BY-NC).

## INTRODUCTION

Topological matter is a rapidly growing field in which topological concepts are exploited to discover and classify new phases of matter (1–4). In this context, a hallmark achievement was the discovery of the integer quantum Hall effect (5). In the past decade, topological phases analogous to quantum Hall insulators have been engineered across a wide range of time-modulated platforms, including electronics (6–8), photonics (9–14), acoustics (15–18), and mechanics (19–24). The existence of the conventional gapless edge states and surface states is guaranteed by the bulk-boundary correspondence. These time-dependent systems can provide outstanding opportunities not possible with passive materials, enabled by the high controllability and flexibility of these platforms. However, a physical realization of a dynamically controlled topological pumping that produces topological transport is extremely challenging because external or active physical fields are typically needed (25).

To overcome the challenges associated with time-modulated system, rendering synthetic dimensions via space modulations was recently suggested because it does not require any active materials or other external mechanisms to break the time-reversal symmetry (26, 27). The phases of the space modulations can be used as adiabatic parameters that augment the physical space. It is intriguing to see these phases as additional global degrees of freedom, usually called phasons, living on a torus. The central idea of synthetic dimensions is to exploit and harness such degrees of freedom with atoms, photons, or phonons to mimic the dynamic motion along extra spatial directions. The key advantage of synthetic dimensions is that pumping parameters can be engineered very naturally in the strength of the couplings along the extra dimension. Synthetic dimensions have led to new discoveries of the two-dimensional (2D) and 4D quantum Hall systems in ultracold atomic gases (28, 29),

photonics (30–32), and acoustics and mechanics (33–35) because of their flexibility. Rendering of the synthetic space is growing into one of the most appealing approaches to control and steer topological wave transport in different systems.

Surface elastic waves are a class of polarized waves that propagate on the surface of a semi-infinite elastic medium. They are confined within a superficial region whose thickness is comparable with their wavelength (36). Manipulating surface waves has been of considerable interest with widespread applications in earthquake mitigation, nondestructive evaluation, wave filtering, and sensing (37–39). On the basis of the Bragg scattering and local resonance mechanisms, manipulation and control of surface waves have been recently investigated in the phononic and metamaterial community for various applications such as exotic wave transmission and reflection, wave focusing, and cloaking (40–42). Among existing approaches, the metamaterial with pillar-type resonators is regarded as one of the most promising microstructure designs because of their simple structure and process-friendly fabrication. However, it is not trivial to apply pillar-type metamaterials for the topological surface wave transport. There is of fundamental and practical significance to physically realize space-modulated pillar-type metamaterials for topological surface wave transport along desired orbits (43, 44).

In this study, we present theoretical, numerical, and experimental investigations of Rayleigh wave topological pumping by leveraging a pillar-based platform with space modulations. The proposed structures can be described as aperiodic mechanical wave channels carrying different phason values that are stacked and coupled with each other. By slowly varying the phason along the stacking direction, we demonstrate here that, with such an approach, we can explore any continuous orbit inside the phason space and even control the speed along the path to shape the surface pumped pattern. As a result, we can render these abstract trajectories, occurring in the synthetic dimensions, on the physical dimension along the stackings. In turn, this enables us to control the propagation of the surface waves in space and the temporal phases of the signals.

With the control over the phason, we experimentally demonstrate edge-to-edge topological wave transport on the space-

<sup>1</sup>Department of Mechanical and Aerospace Engineering, University of Missouri, Columbia, MO 65211, USA. <sup>2</sup>School of Aerospace Engineering, Beijing Institute of Technology, Beijing 100081, China. <sup>3</sup>Piezoelectric Device Laboratory, School of Mechanical Engineering and Mechanics Ningbo University, Ningbo 315211, China. <sup>4</sup>Department of Physics, Yeshiva University, New York, NY 10016, USA.

\*Corresponding author. Email: ruizhu@bit.edu.cn (R.Z.); huangg@missouri.edu (G.H.)

†These authors contributed equally to this work.

modulated mechanical metasurface, which is robust against random fluctuations in the couplings. The analytical study of pumping process under adiabatic condition is formulated by using the Wentzel-Kramers-Brillouin (WKB) approximation and the modulation functions of parameters with nontrivial topological phases are also analytically obtained. On the basis of that, we further explore various ways in which we can control these pumping processes and validate topological mode steerings in time domain simulation. It is believed that our work breaks ground for engineering applications, where the couplings in a space-modulated mechanical metasurface can be programmed for selective and robust point-to-point transport of surface wave signals.

## RESULTS

### Physical rendering of synthetic spaces

We start by explaining the principles of physical rendering of synthetic spaces in the context of surface wave transport. Figure 1 (A and B) shows our surface wave platform featuring a planar array of elastic pillar-type resonators coupled horizontally and vertically through thin plates (see Materials and Methods for fabrication details). Each resonator is assigned an address  $(i,j) \in \mathbb{Z}^2$  in the  $x$ - $z$  plane. The heights of the connecting plates in the  $x$  direction are modulated according to the protocol  $h_{ij} = h_0[1 + \Delta_0 \cos(2\pi i/3 + \phi_j)]$ , while the geometry of the connecting thin plate along the  $z$

direction is uniform across the sample. Any such modulation has a phase that can take any value in the abstract interval  $[0, 2\pi]$ , representing here the synthetic space. In a time-modulated setting, one will dynamically drive the phase  $\phi$  by rapid reconfigurations of the systems (45). Instead, by setting the phason value of the  $j$ -th row as  $\phi_j = \phi_s + (\phi_f - \phi_s) \frac{j}{N}$ , with  $N$  being the total number of rows, we effectively render the synthetic space along the  $z$  axis. The parameters will be fixed as  $\phi_s = 0.6\pi$  and  $\phi_f = 1.4\pi$ .

As shown in Fig. 1A, each  $x$  directional row displays a unit cell containing three pillars. The dispersion curves of the unit cell obtained with COMSOL Multiphysics are shown in Fig. 1C. The computation was carried out by imposing Floquet boundary conditions in both  $x$  and  $z$  directions. Because the modulation amplitude  $\Delta_0$  is small,  $\phi_j$  is irrelevant for the dispersion curves and can be assumed as 0. Below the sound cone (white region), one can see three surface wave branches, whose eigenmodes are localized on the surface and decay quickly into the bulk (see the Supplementary Materials). The region above the sound cone, shown in gray, is referred to as the "bulk modes" region.

To facilitate the physical interpretation of the surface wave pumping and illuminate the function of the phason, we develop a discrete mass-spring model for the surface wave eigenmodes using the mode-coupling theory. This model takes the form of the following difference equation for the amplitudes  $\psi_{ij}$  of the local

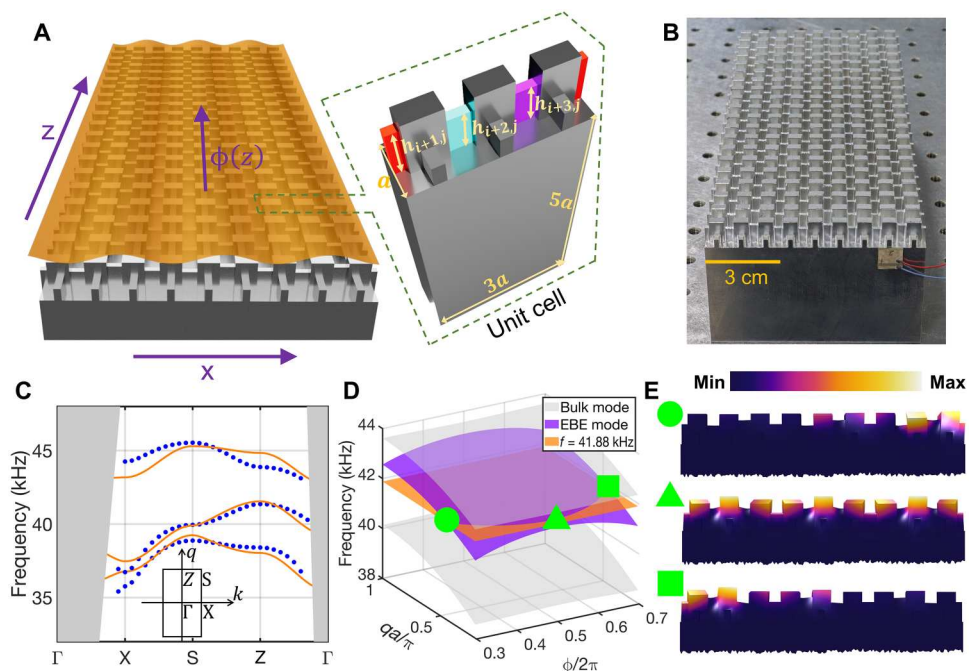


**Fig. 1. Design principle and dispersion analysis.** (A) Schematic illustration of the topological surface wave transport system. Each row in  $x$  corresponds to a supercell that includes three unit cells (inset). (B) Photograph of the experimental sample fabricated out of aluminum by a milling machine. The piezoelectric actuator on the bottom right serves as the excitation. (C) Numerically obtained dispersion curves (blue dots) for the unit cell with  $\phi_j = \pi$ . The orange curves represent the dispersion curves of the discrete mass-spring model obtained by numerical fitting. The gray regions are filled with bulk modes. Their interfaces with the surface wave region define the sound cone. (D) Dispersion diagram for the supercell terminated by free boundary conditions in the  $x$  direction and Floquet boundary conditions in the  $z$  direction. The edge-bulk-edge (EBE) mode is represented by the magenta surface, whereas the bulk bands are indicated by gray surfaces. The orange cut plane corresponds to the excitation frequency  $f_c = 41.88$  kHz. The interaction curve between excitation frequency plane and EBE surface gives the instantaneous wave number  $q(z)$  on which the circle is right edge mode, the triangle is the bulk mode, and the square is the left edge mode. (E) The top, middle, and bottom panels are the corresponding eigenmodes of supercell at  $\phi = 0.6\pi$  (circle),  $\pi$  (triangle), and  $1.4\pi$  (square) with  $q = \pi/a$  in (D).

resonances carried by the individual pillars (see the Supplementary Materials)

$$\begin{aligned} \kappa^0 \psi_{i,j} + \kappa_{i-1,j}^h \psi_{i-1,j} + \kappa_{i,j}^h \psi_{i+1,j} + \kappa^v [\psi_{i,j-1} - 2\psi_{i,j} + \psi_{i,j+1}] \\ = -M\tilde{\omega}^2 \psi_{i,j} \end{aligned} \quad (1)$$

Here,  $M$ ,  $\tilde{\omega}$ ,  $\kappa^0$ ,  $\kappa^v$ , and  $\kappa^h$  are interpreted as the effective mass; angular frequency; and grounded, vertical, and horizontal spring stiffnesses of the model, respectively. The values of these effective parameters are determined by fitting the dispersion curves of the continuous model (blue dots in Fig. 1C). Specifically, we obtain  $M = 1$  kg,  $\kappa^0 = 49.6$  GN/m,  $\kappa^v = 1.9$  GN/m, and  $\kappa_{i,j}^h = \kappa_0^h [1 + \Delta \cos(2i\pi/3 + \phi_j)]$ , where the modulation coefficients read  $\kappa_0^h = 5.5$  GN/m and  $\Delta = 0.67$ . As shown in Fig. 1C, the continuous and discrete dispersion curves exhibit satisfactory agreement, thereby demonstrating the reliability of the discrete model.

### WKB-type analysis

By replacing the index  $j$  with the coordinate  $z = ja$ , we rewrite  $\psi_{i,j} = \psi_i(z)$  and  $\phi_j = \phi(z)$ , as well as

$$\kappa_{i,j}^h = \kappa_i^h(z) = h_0 \left\{ 1 + \Delta \cos \left[ \frac{2\pi i}{3} + \phi(z) \right] \right\} \quad (2)$$

We also introduce the second-order central difference operator

$$\delta^2 f(z) = \frac{f(z+a) - 2f(z) + f(z-a)}{a^2} \quad (3)$$

In addition, a vector  $\psi(z) = [\psi_0(z), \psi_1(z), \dots, \psi_{3M}(z)]^T$  is defined including all the mode coefficients. By doing so, the dispersion equation (Eq. 1) can be written very compactly as

$$a^2 \delta^2 \psi(z) + [\mathbf{K}(z) + \omega^2] \psi(z) = 0 \quad (4)$$

in which normalized angular frequency  $\omega$  satisfies  $\omega^2 = \tilde{\omega}^2/\kappa^v$  and  $\mathbf{K}(z)$  is the matrix with the entries

$$K_{ik}(z) = [\kappa^0 \delta_{ik} + \kappa_i^h(z) \delta_{i,k+1} + \kappa_i^h(z) \delta_{i+1,k}] / \kappa^v \quad (5)$$

where  $\delta_{ik}$  is the Kronecker delta. Equation 4 is very close in spirit with the Schroedinger equation appearing in the setting of WKB approximation theory (46, 21). The difference is that, instead of dealing with a potential, we are dealing with the nondiagonal matrix  $\mathbf{K}(z)$ , which, nevertheless, is slowly varying with  $z$ . In this regime, the following WKB-type expansion is justified

$$\psi(z) = e^{i\theta(z)/a} [\psi^{(0)}(z) + a\psi^{(1)}(z) + \dots] \quad (6)$$

and, by keeping track of the powers of  $a$ , we can derive the exact equations satisfied by each  $\psi^{(a)}$ . In particular, we find for the leading term that this equation is (see the Supplementary Materials)

$$[\mathbf{K}(z) + \omega^2] \psi^{(0)}(z) = 4 \sin^2 \left[ \frac{\delta\theta(z)}{2} \right] \psi^{(0)}(z) \quad (7)$$

where  $\delta\theta(z) = [\theta(z+a/2) - \theta(z-a/2)]/a$ . This equation has solutions of the form

$$\psi_n(z) = A_n(z) e^{i \sum_{\xi=0}^{z} q_n(\xi)} \varphi_n(z) + o(a) \quad (8)$$

where  $\varphi_n(z)$  is the  $n$ -th eigenmode of the  $\mathbf{K}(z)$  matrix

$$\mathbf{K}(z) \varphi_n(z) = -\mu_n(z) \varphi_n(z) \quad (9)$$

at row  $z$  and  $q_n(z)$  satisfies the equation

$$4 \sin^2 \frac{q_n(z)}{2} + \mu_n(z) = \omega^2 \quad (10)$$

As in the standard WKB theory (46), an analysis at the order-one level of the asymptotic expansion enables us to pinpoint the  $z$ -dependence amplitude  $A_n(z)$  (see the Supplementary Materials) and to lastly present the complete set of solutions for the dispersion (Eq. 4)

$$\psi_n(z) = \frac{c_n}{\sqrt[4]{\omega^2 - \mu_n(z)}} e^{i \sum_{\xi=0}^{z} q_n(\xi)} \varphi_n(z) + o(a) \quad (11)$$

We recall that the derivation of these solutions relies only on the adiabatic evolution of the phason with  $z$  and no considerations of long wavelengths or paraxial approximation were made. Thus, our results cover the short-wavelength and nonparaxial regions. Last, because our samples are finite, we need to impose free boundary conditions on the top and bottom boundaries in the  $z$  direction. In this case, the mode shape of the  $n$ -th eigenmode is in the form of

$$\psi_n(z) = \frac{c_n \sin Q_n(z) + d_n \cos Q_n(z)}{\sqrt[4]{\omega_n^2 - \mu_n(z)}} \varphi_n(z) \quad (12)$$

where  $c_n$  and  $d_n$  are coefficients of superposition,  $\omega_n$  is the eigenfrequency, and  $Q_n(z) = \sum_{\xi=0}^{z} q_n(\xi)$  is the dynamical phase produced by our derivation.

### Topological pumping

The complete set of solutions (Eq. 11) indicates that, when the metasurface is excited at pulsation  $\omega$  with a source placed at position  $z = 0$ , it will resonate very strongly with the mode that has its resonant frequency  $\mu_n(z=0)$  close to  $\omega^2$ . Thus, we have a mechanism to selectively load a specific mode out of a fairly rich set of resonant modes. Furthermore, Eq. (11) indicates that, with such a source turned on, upon the inspection of row  $z$ , we will see the eigenmode  $\varphi_n(z)$  of the 1D tight-binding operator  $\mathbf{K}(z)$  (up to a multiplicative factor). Because  $\mathbf{K}(z)$  depends only on the phason value  $\phi(z)$ , i.e.,  $\mathbf{K}(z) = \mathbf{K}_{\phi(z)}$ , one can now see explicitly how the dependence of the spectral properties of  $\mathbf{K}_{\phi}$  on the phason has been rendered along the  $z$  coordinate, for us to experience, measure and use its resonant modes in future applications. Furthermore, by design, the phason is being pumped from  $\phi_s$  to  $\phi_f$  as the structure is examined from bottom ( $z = 0$ ) to the top ( $z = Na$ ).

The spectrum of an entire row of resonators  $q$ -twisted Floquet boundary conditions imposed in the  $z$  direction is reported in Fig. 1D as a function of  $\phi$  and  $q$ , and the topological edge modes can be seen as the sheet colored in magenta. Taking a slice at a fixed  $q$  reveals precisely one chiral edge band per edge and the slopes of these bands are consistent with the values of the Chern numbers (see the Supplementary Materials). Furthermore, examination of the eigenfunctions leads to the observation of right edge, bulk, and left edge modes for  $\phi = 0.6\pi$ ,  $\pi$ , and  $1.4\pi$  in the top, middle, and bottom panels of Fig. 1E, respectively.

## Demonstration of topological surface wave transport

We now focus on the demonstration of the topological surface wave transport. Experiments are first conducted on the system shown in Fig. 1 (A and B). Figure 2 (A and B) illustrates the magnitude of  $y$  directional displacement fields of the edge-bulk-edge (EBE) mode from experiments at 42.45 kHz and from numerical simulations at 41.88 kHz, respectively. As a matter of fact, the measurement of the  $y$  component is essentially equivalent to that of the  $z$  component because the  $y$  component has measurable intensity and displays the same spatial profiles of the EBE mode as the  $z$  component because of their linear relationship (see the Supplementary Materials). In addition, the experimentally measured frequency of the EBE mode could be different from the simulated eigenfrequency because of fabrication and material imperfections. To precisely determine the EBE frequency in the experiment, we perform a thorough analysis of the frequency spectra derived from measurements taken at the resonator with  $i = 2$  and  $j = 18$ , as shown in Fig. 2C. After deliberately examining the mode shapes in each resonance peak, we can determine the experimental EBE frequency as 42.45 kHz. It is worth mentioning that frequency spectra measured at other locations also exhibit the same resonance peaks as observed in the case of  $i = 2$  and  $j = 18$ , albeit with different intensities (see the Supplementary Materials). In other words, selecting different locations for frequency response measurements results in the identical observation of the EBE mode. As shown in Fig. 2 (A and B), vertical oscillation of the field profile in  $z$  is observed featured with modal

nodes and antinodes, owing to the  $z$ -directional dynamical phase. The experimental and numerical results provide satisfactory agreement. To quantitatively compare the retrieved mode profile in Fig. 2B with the analytical solution (Eq. 12), we apply wavelet transform and mode decomposition on the numerical mode profile. In detail, we first divided the cuboid into nine columns. Then, the wavelet transform technique is applied to the wave component of each column to determine the corresponding coefficients. Last, we calculate the average of the absolute values for these coefficients. The outcome after linear interpolation is illustrated as a heatmap in Fig. 2D. As a reference, a purple curve is given to provide the  $q\phi$  relation at 41.88 kHz on the cut plane of the dispersion diagram (Fig. 1D). Satisfactory agreement is found between the eigenmode analysis of the finite lattice and the dispersion diagram. Next, we adopt mode decomposition on each of the 20 supercells along the  $z$  direction to determine the relative strengths of all modes. Figure 2E illustrates the corresponding modal coefficients that are normalized with the maximum of coefficient at respective values of  $z$ . The bases for mode decomposition are from the corresponding mass-spring model whose parameters are extracted from Fig. 1C. Because only 20 supercells are involved in the synthetic dimension, the stiffness matrix does not evolve strictly adiabatically. As a result, other bulk modes always coexist. However, the EBE mode, labeled as the seventh mode in Fig. 2E, is always dominant in terms of modal coefficients of all the supercells, meaning that the length of the synthetic dimension is sufficiently long to approach adiabatic

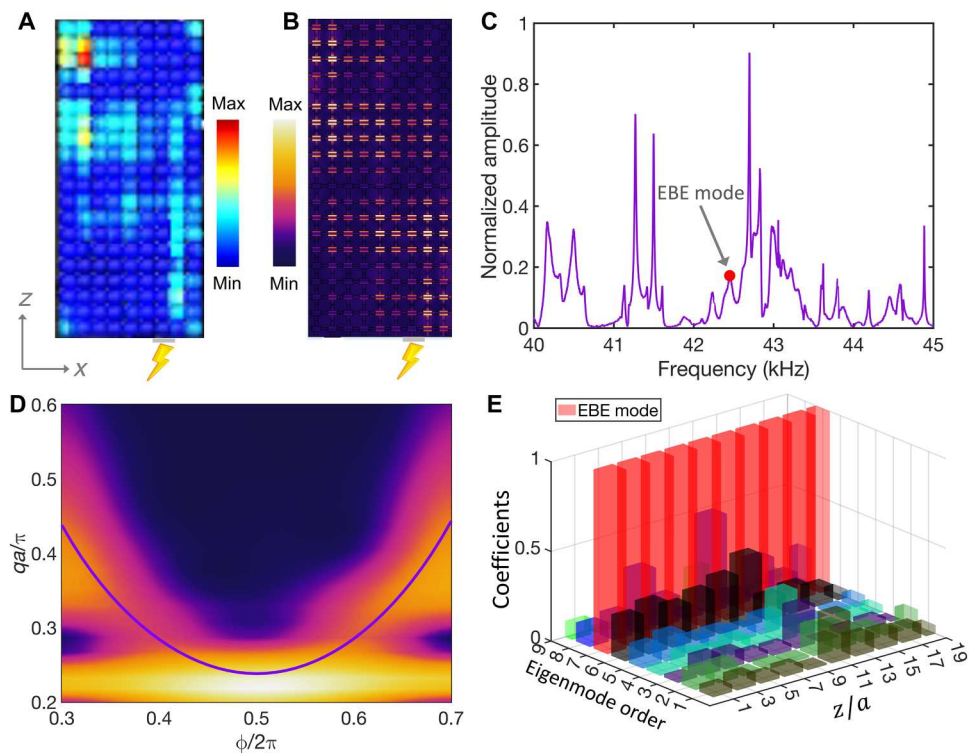


**Fig. 2. Topological surface pumping on the elastic surface with space modulated pillars.** (A and B) Experimental (A) and numerical (B) modal profile of the magnitude of the  $y$  directional (out-of-plane) displacement field at the frequencies  $f = 42.45$  kHz and  $f = 41.88$  kHz, respectively, by a piezoelectric patch (gray part in the bottom of the cuboid) excitation. (C) Frequency spectrum of the resonator with indices  $i = 2$  and  $j = 18$  from experimental measurement. The resonance peak noted by red dot is the EBE mode. (D) The wavelet transform of the eigenmode from numerical simulation along synthetic dimension. The purple curve is the interaction curve from Fig. 1D. (E) The mode decomposition of the displacement field in (B) of each chain for different  $z$ .

limit. The consistency of the results from wavelet transform and mode decomposition analysis validates the correctness of the WKB solution. Moreover, it is noteworthy to mention that the topological pumping can occur at multiple frequencies, in addition to the frequency that we have experimentally demonstrated (see the Supplementary Materials). In the current design, the frequency range to exhibit the topological pumping is approximately 1 kHz, as evidenced by the frequency span of the magenta EBE surface (Fig. 1D). To broaden the frequency range of the topological pumping, one possibility to explore is the improvement of stiffness of the connecting plates in the  $z$  direction. This adjustment would result in the EBE surface at a broader frequency range.

We conduct the transient analysis for better showcasing the pumping process. In particular, the right edge mode  $\varphi_n(0)$  ( $n = 7$ ) at the bottom supercell is excited by using a series of piezoelectric patches, each attached on one side of each resonator (see Materials and Methods). The polarization directions of these piezoelectric patches are identical, while the applied voltages are distributed as  $V_0\varphi_n(0)f_z(t)$ , where  $V_0 = 1$  V denotes the voltage amplitude and  $f_z(t)$  is a 50-cycle tone burst signal  $f_z(t) = H(50/f_c - t)[1 - \cos(2\pi f_c t/50)] \sin(2\pi f_c t)$  (Fig. 3, top), with  $H(t)$  being the Heaviside function and  $f_c = 41.88$  kHz. Figure 3 (A to C) displays the snapshots of surface wave propagation at representative time instants in terms of the magnitude of total displacement field. It should be mentioned that the total displacement field is very similar to its  $z$  directional component according to our numerical simulation. Initially, the right edge mode is excited on the bottom at  $t = 0.5$  ms (Fig. 3A). As time progresses, the wave packet propagates in the synthetic dimension  $z$  and transitions into the bulk mode at  $t = 2.5$  ms (see Fig. 3B). Eventually, the left edge mode is well formed on the top of the cuboid at  $t = 4$  ms (Fig. 3C). The wave packet will follow the same evolution path transitioning from the left edge mode back to the right one if the transient simulation continues. A more detailed demonstration can be found in movie S1.

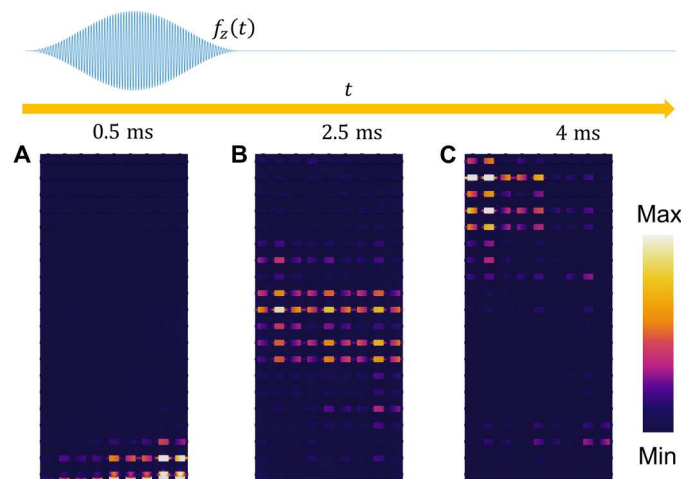


**Fig. 3. Time response of the topological surface wave transport.** (A to C) The magnitude of total displacement field at 0.5 ms, 2.5 ms, and 4 ms, respectively. A 50-cycle tone burst signal centered at 41.88 kHz is simulated on the bottom supercell.

## Robustness of topological surface wave transport

The geometric imperfections in sample fabrication are inevitable because of the errors of millers of computer numerical control (CNC) machines, as minor discrepancies between simulations and measurement are visible in Fig. 2 (A and B). Nevertheless, the topological surface wave transport is evidently observed, thanks to some intriguing wave transport characteristics, such as robustness against geometrical impurities or defects. To illustrate this, Fig. 4A shows a lattice defect constructed by removing 3  $\times$  3 pillars in the middle of the structure. The corresponding eigenfrequency of the EBE mode of the defective cuboid (41.75 kHz) is quite close to that of a perfect cuboid (41.88 kHz). The resulting spatial profile shows that the topological pumping behavior survives and the edge modes can be smoothly pumped from one side to the other despite the large-scale geometric defect. Numerical analysis is also conducted showing that large-scale defects at different positions have minimal impact on the transport of the EBE mode, indicating its topological robustness irrespective of the defect's location (see the Supplementary Materials). Moreover, we also consider the influence of geometrical disorders. In the sample fabrication, the machining error is about 0.02 mm for our sample. Therefore, we introduce errors that satisfy a normal distribution  $\mathcal{N}(0 \text{ mm}, 0.02 \text{ mm})$  to the dimensions of all resonators, including their lengths, heights, and widths. The spatial profile of the EBE mode with disorders is shown in Fig. 4B. The eigenfrequency of the EBE mode shifts slightly, and the spatial profile agrees with that of the perfect lattice in the  $x$  direction, indicating that the topological pumping is robust against disorders. However, in the  $z$  direction, we see that amplitudes of resonators in the top part are larger than amplitudes of resonators in the bottom part, which is a sign of Anderson localization. Because along the  $z$  direction, the displacement field is harmonic, and the disorders make the eigenmode localized at the top. It is also observed in the experiment (Fig. 2A) that the eigenmode is localized at the top. Numerical simulations indicate that the wave transport efficiency is nearly perfect, approaching unity if the low damping factor of the material is considered, which is also in good agreement with our experimental measurement (see the Supplementary Materials). Therefore, the

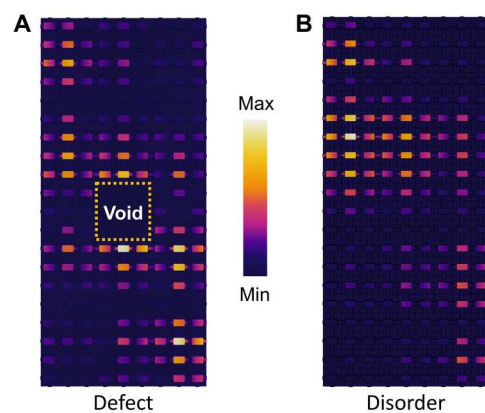


**Fig. 4. Robust topological surface wave pumping.** (A) The eigenmode of the defective structure at 41.75 kHz. The defect is constructed by removing 3 by 3 pillars in the dotted line box (B) The eigenmode of the disordered structure where a random normal distribution of errors is added on all geometric parameters at 41.88 kHz.

energy consumption associated with wave transport can be ignored in the present passive system.

### Application of topological wave transport as wave splitter

Surface wave topological pumping is promising for controlling wave paths in practical applications. To show that, we design a topological split-flow device that performs robust surface wave splitting. Other topological pumping patterns with more complicated paths can be engineered through selecting different phason trajectories (see the Supplementary Materials). As shown in Fig. 5A, the splitter is an assembly of two domains with opposite  $\phi$ -z distributions, separated by a domain wall (yellow in Fig. 5A). Specifically, the upper section with 20 supercells of the left domain is designed with a linear  $\phi$  transition from  $0.6\pi$  to  $1.4\pi$ , whereas that of the right domain is assigned an opposite  $\phi$  transition, i.e., from  $1.4\pi$  to  $0.6\pi$ . As for the lower section with three supercells,  $\phi$  keeps constant at  $0.6\pi$  and  $1.4\pi$  for the left and right domains, respectively. The excitation is located in the middle of the bottom. Within the lower section of the surface wave splitter, there exists a localized interface mode. As the incidence reaches the upper half, because of the opposite gradients of  $\phi$ , the interface mode is split into two components, each following the typical EBE evolution but tracing opposite paths. Thanks to topological protection, the propagation is immune against back reflection from the discontinuity of the upper and lower sections. Hence, our design, based on phason engineering and topological pumping, provides an avenue for the application of elastic surface wave beam splitters. In addition, our design covers the short-wavelength range such that we have the opportunity to engineer the dispersion with respect to  $q$  quasi-momentum. This involves modulations along the vertical direction and opens up a new dimension in the design space for surface wave, which is yet to be explored.

### DISCUSSION

In conclusion, we have evidenced the topological surface wave transport in modulated phononic crystals through edge-to-edge topological pumpings associated with the 2D quantum Hall effects by the physical rendering of synthetic spaces. These observations imply

that the system is characterized by a non-zero Chern number, and therefore, the topological pumping is immune to bulk scattering and exhibits strong protection against design imperfections. The modulated phononic crystals with synthetic spaces offer a platform and route for efficient surface wave topological mode transport by engineering desired patterns on a phason-torus in the finite structure. The phason space augments the physical space and opens a door to higher-dimensional physics in acoustics and mechanics. Although we focused on the elastic implementation using synthetic spaces, our approach can be generalized to other degrees of freedom, such as additional frequency dimensions can also be harnessed for the frequency modulation. Going forward, it will be important to develop and explore such broader connections, as the idea of topological matter in synthetic dimensions is very general and the extension of this approach to other complex orbits is much awaited. At last, we emphasize that, to achieve a reasonable adiabatic regime, the number of chains in our experimental setups is appreciable, and while this is perfectly fine for the demonstration purposes, it could be an obstacle for practical applications. It will be interesting to explore if this strategy can be deployed for our phononic crystals to reduce the number of chains needed for the topological pumping of surface wave.

### MATERIALS AND METHODS

#### Sample fabrication

The experimental sample made of aluminum, having Young's module  $E = 69$  GPa, Poisson's ratio  $\nu = 0.33$ , and density  $\rho = 2700$  kg/m<sup>3</sup>, is fabricated using the computer numerical control (CNC) milling machine with a manufacturing precision of 0.02 mm. It consists of an array of resonators (6 mm × 3.5 mm × 10 mm) with the number of 9 along the x-direction and 20 along the z direction, which are integrated with a cuboid (150 mm by 50 mm by 200 mm). For convenience, each resonator has an address  $(i,j)$ . Along the x direction, resonators  $(i,j)$  and  $(i+1,j)$  are connected by height-modulated pillars (4 mm by 1.5 mm by  $h_{ij}$ ), which satisfy the protocol  $h_{ij} = h_0[1 + \Delta_0 \cos(2\pi i/3 + \phi_j)]$ , where  $h_0 = 7$  mm and  $\Delta_0 = 0.15$  is the average thickness of horizontal channels. Besides,  $\phi_j = \phi_s + (\phi_f - \phi_s)j/N$ , where  $\phi_s = 0.6\pi$ ,  $\phi_f = 1.4\pi$ , and  $N = 20$ . In the z direction, all resonators are connected by pillars of the same size (2 mm by 6.5 mm by 3.8 mm).

#### Experimental testing

In the experiment, the sample is supported by four points to mimic the free boundary condition. A piezoelectric ceramic patch is attached to the right side of the cuboid to excite the target eigenmode state. A wide-spectrum pseudo-random excitation within the probing ranges from 20 to 50 kHz is generated by a Tektronix AFG3051C arbitrary waveform generator and amplified by a Krohn-Hite high-voltage power amplifier, which is lastly applied across the piezoelectric source. A 1D scanning laser Doppler vibrometer (SLDV, Polytech PSV-500) is used to measure the vibration velocity of resonators in the y direction, where high-gain reflective tape is stuck on the surface of each resonator to enhance the reflection of the laser. The piezoelectric actuators located on the bottom supercell are used for excitation. The decision to measure the y component instead of the dominant z component is motivated by the presence of neighboring resonators within the measurement area, which inevitably obstruct the scanning laser of the 1D laser

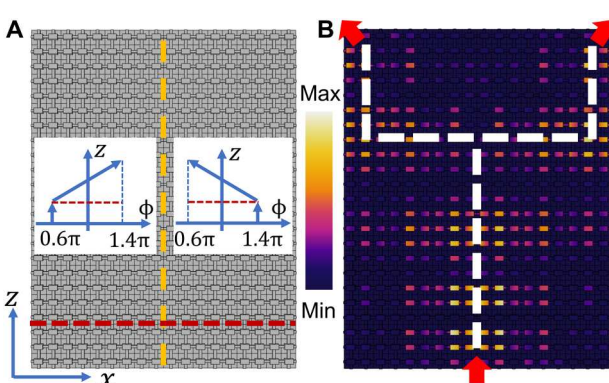


**Fig. 5. Topologically protected surface wave splitter.** (A) The schematic of surface wave pumping system and the corresponding phase modulation functions. (B) The magnitude of total displacement field distribution of the surface wave splitter. The surface wave is injected at the center of the bottom edge at the frequency  $f = 41.88$  kHz.

vibrometer (PSV-500). Consequently, physically measuring the  $z$  component becomes experimentally unfeasible. To ensure satisfactory measurement accuracy and consistency of the  $y$  directional displacements across different pillars, we carefully select the middle point  $[x = \frac{(2i-1)a}{2}, y = a, z = \frac{t_0}{2} + ja - \varepsilon]$  along one edge of the top surface of each pillar as the measurement point, where  $i = 1, 2, \dots, 9, j = 1, 2, \dots, 20$  are the pillar indices, and  $\varepsilon$  is the radius of the laser spot approximately equal to 0.25 mm (see the Supplementary Materials). The velocity signal from the vibrometer is further recorded by the PSV-500 data acquisition. Note that the experiment is repeated and averaged five times on each resonator of the system to filter out part of the noise. The normalized amplitude spectrum obtained by applying the Fourier transform to the time-domain signals collected at the resonator (2,18) is shown in Fig. 2C. A series of resonant peaks are observed in the frequency range. By checking the mode shape of each resonance peak in the frequency spectrum, the EBE state corresponding to the frequency at 42.45 kHz is identified. Moreover, a full field measurement at 42.45 kHz is conducted by exciting the system with a harmonic sine excitation, and the same EBE state is measured.

### Numerical simulations

The full-wave finite-element method simulations in this work are all performed using the commercial software COMSOL Multiphysics. The material of 3D structure is implemented by Aluminum [solid] from COMSOL Material Library. Eigenfrequency analysis within the "Solid Mechanics" is carried out to calculate the eigenfrequencies and eigenmode of the unit cell, supercell, and cuboid. The boundary conditions for all the cases are set as free boundary conditions except for Floquet periodicity boundary conditions of the unit cell along  $x$  and  $z$  direction and of the supercell along  $z$  direction. For the transient analysis in Fig. 3, time-dependent analysis in the Solid Mechanics is used. Piezoelectric patches (PZT-5H in COMSOL Material Library) are attached on one side of each resonator of the bottom supercell. The polarization directions of these piezoelectric patches are identical, while the applied voltages are distributed as  $V_0\Phi_n(0)f_z(t)$ .

### Supplementary Materials

#### This PDF file includes:

Supplementary Text

Figs. S1 to S9

Table S1

Legend for movie S1

#### Other Supplementary Material for this manuscript includes the following:

Movie S1

### REFERENCES AND NOTES

- M. Z. Hasan, C. L. Kane, Colloquium: Topological insulators. *Rev. Mod. Phys.* **82**, 3045 (2010).
- X.-L. Qi, S.-C. Zhang, Topological insulators and superconductors. *Rev. Mod. Phys.* **83**, 1057 (2011).
- C.-K. Chiu, J. C. Y. Teo, A. P. Schnyder, S. Ryu, Classification of topological quantum matter with symmetries. *Rev. Mod. Phys.* **88**, 035005 (2016).
- S. Rachel, Interacting topological insulators: A review. *Rep. Prog. Phys.* **81**, 116501 (2018).
- K. V. Klitzing, G. Dorda, M. Pepper, New method for high-accuracy determination of the fine-structure constant based on quantized hall resistance. *Phys. Rev. Lett.* **45**, 494 (1980).
- N. H. Lindner, G. Refael, V. Galitski, Floquet topological insulator in semiconductor quantum wells. *Nat. Phys.* **7**, 490–495 (2011).
- Y. Xu, I. Miotkowski, C. Liu, J. Tian, H. Nam, N. Alidoust, J. Hu, C.-K. Shih, M. Z. Hasan, Y. P. Chen, Observation of topological surface state quantum hall effect in an intrinsic three-dimensional topological insulator. *Nat. Phys.* **10**, 956–963 (2014).
- R. Yoshimi, A. Tsukazaki, Y. Kozuka, J. Falson, K. S. Takahashi, J. G. Checkelsky, N. Nagaosa, M. Kawasaki, Y. Tokura, Quantum hall effect on top and bottom surface states of topological insulator  $(\text{Bi}_{1-x}\text{Sb}_x)_2\text{Te}_3$  films. *Nat. Commun.* **6**, 6627 (2015).
- F. D. M. Haldane, S. Raghu, Possible realization of directional optical waveguides in photonic crystals with broken time-reversal symmetry. *Phys. Rev. Lett.* **100**, 013904 (2008).
- Z. Wang, Y. Chong, J. D. Joannopoulos, M. Soljačić, Observation of unidirectional back-scattering-immune topological electromagnetic states. *Nature* **461**, 772–775 (2009).
- M. C. Rechtsman, J. M. Zeuner, Y. Plotnik, Y. Lumer, D. Podolsky, F. Dreisow, S. Nolte, M. Segev, A. Szameit, Photonic floquet topological insulators. *Nature* **496**, 196–200 (2013).
- M. Hafezi, S. Mittal, J. Fan, A. Migdall, J. M. Taylor, Imaging topological edge states in silicon photonics. *Nat. Photonics* **7**, 1001–1005 (2013).
- L. Lu, J. D. Joannopoulos, M. Soljačić, Topological photonics. *Nat. Photonics* **8**, 821–829 (2014).
- T. Ozawa, H. M. Price, A. Amo, N. Goldman, M. Hafezi, L. Lu, M. C. Rechtsman, D. Schuster, J. Simon, O. Zilberberg, I. Carusotto, Topological photonics. *Rev. Mod. Phys.* **91**, 015006 (2019).
- R. Fleury, A. B. Khanikaev, A. Alù, Floquet topological insulators for sound. *Nat. Commun.* **7**, 11744 (2016).
- Z. Yang, F. Gao, X. Shi, X. Lin, Z. Gao, Y. Chong, B. Zhang, Topological acoustics. *Phys. Rev. Lett.* **114**, 114301 (2015).
- S. H. Mousavi, A. B. Khanikaev, Z. Wang, Topologically protected elastic waves in phononic metamaterials. *Nat. Commun.* **6**, 8682 (2015).
- A. Souslov, B. C. Van Zuiden, D. Bartolo, V. Vitelli, Topological sound in active-liquid metamaterials. *Nat. Phys.* **13**, 1091–1094 (2017).
- P. Wang, L. Lu, K. Bertoldi, Topological phononic crystals with one-way elastic edge waves. *Phys. Rev. Lett.* **115**, 104302 (2015).
- L. M. Nash, D. Kleckner, A. Read, V. Vitelli, A. M. Turner, W. T. M. Irvine, Topological mechanics of gyroscopic metamaterials. *Proc. Natl. Acad. Sci. U.S.A.* **112**, 14495–14500 (2015).
- H. Nassar, H. Chen, A. N. Norris, G. L. Huang, Quantization of band tilting in modulated phononic crystals. *Phys. Rev. B* **97**, 014305 (2018).
- H. Chen, L. Y. Yao, H. Nassar, G. L. Huang, Mechanical quantum hall effect in time-modulated elastic materials. *Phys. Rev. Appl.* **11**, 044029 (2019).
- M. I. N. Rosa, R. K. Pal, J. R. F. Arruda, M. Ruzzene, Edge states and topological pumping in spatially modulated elastic lattices. *Phys. Rev. Lett.* **123**, 034301 (2019).
- E. Riva, M. I. N. Rosa, M. Ruzzene, Edge states and topological pumping in stiffness-modulated elastic plates. *Phys. Rev. B* **101**, 094307 (2020).
- I. H. Grinberg, M. Lin, C. Harris, W. A. Benalcazar, C. W. Peterson, T. L. Hughes, G. Bahl, Robust temporal pumping in a magneto-mechanical topological insulator. *Nat. Commun.* **11**, 974 (2020).
- M. Lohse, C. Schweizer, H. M. Price, O. Zilberberg, I. Bloch, Exploring 4d quantum hall physics with a 2d topological charge pump. *Nature* **553**, 55–58 (2018).
- O. Zilberberg, S. Huang, J. Guglielmon, M. Wang, K. P. Chen, Y. E. Kraus, M. C. Rechtsman, Photonic topological boundary pumping as a probe of 4d quantum hall physics. *Nature* **553**, 59–62 (2018).
- H. M. Price, O. Zilberberg, T. Ozawa, I. Carusotto, N. Goldman, Four-dimensional quantum hall effect with ultracold atoms. *Phys. Rev. Lett.* **115**, 195303 (2015).
- M. Lohse, C. Schweizer, O. Zilberberg, M. Aidelsburger, I. Bloch, A Thouless quantum pump with ultracold bosonic atoms in an optical superlattice. *Nat. Phys.* **12**, 350–354 (2016).
- Y. E. Kraus, Y. Lahini, Z. Ringel, M. Verbin, O. Zilberberg, Topological states and adiabatic pumping in quasicrystals. *Phys. Rev. Lett.* **109**, 106402 (2012).
- Y. E. Kraus, Z. Ringel, O. Zilberberg, Four-dimensional quantum hall effect in a two-dimensional quasicrystal. *Phys. Rev. Lett.* **111**, 226401 (2013).
- M. Verbin, O. Zilberberg, Y. Lahini, Y. E. Kraus, Y. Silberberg, Topological pumping over a photonic fibonacci quasicrystal. *Phys. Rev. B* **91**, 064201 (2015).
- H. Chen, H. Zhang, Q. Wu, Y. Huang, H. Nguyen, E. Prodan, X. Zhou, G. Huang, Creating synthetic spaces for higher-order topological sound transport. *Nat. Commun.* **12**, 5028 (2021).
- Y. Long, J. Ren, Floquet topological acoustic resonators and acoustic Thouless pumping. *J. Acoust. Soc. Am.* **146**, 742–747 (2019).
- Z.-G. Chen, W. Tang, R.-Y. Zhang, Z. Chen, G. Ma, Landau-Zener transition in the dynamic transfer of acoustic topological states. *Phys. Rev. Lett.* **126**, 054301 (2021).
- L. Rayleigh, On waves propagated along the plane surface of an elastic solid. *Proc. Lond. Math. Soc.* **s1-17**, 4–11 (1885).

37. C. Campbell, *Surface Acoustic Wave Devices and Their Signal Processing Applications* (Elsevier, 2012).
38. D. Morgan, *Surface Acoustic Wave Filters: With Applications to Electronic Communications and Signal Processing* (Academic Press, 2010).
39. K.-Y. Hashimoto, K.-Y. Hashimoto, *Surface Acoustic Wave Devices in Telecommunications* (Springer, 2000), vol. 116.
40. Y. Jin, B. Bonello, R. P. Moiseyenko, Y. Pennec, O. Boyko, B. Djafari-Rouhani, Pillar-type acoustic metasurface. *Phys. Rev. B* **96**, 104311 (2017).
41. P. Packo, A. N. Norris, D. Torrent, Inverse grating problem: Efficient design of anomalous flexural wave reflectors and refractors. *Phys. Rev. Appl.* **11**, 014023 (2019).
42. Q. Wu, H. Chen, H. Nassar, G. Huang, Non-reciprocal rayleigh wave propagation in space-time modulated surface. *J. Mech. Phys. Solids* **146**, 104196 (2021).
43. J.-Q. Wang, Z.-D. Zhang, S.-Y. Yu, H. Ge, K.-F. Liu, T. Wu, X.-C. Sun, L. Liu, H.-Y. Chen, C. He, M.-H. Lu, Y.-F. Chen, Extended topological valley-locked surface acoustic waves. *Nat. Commun.* **13**, 1324 (2022).
44. Z.-D. Zhang, S.-Y. Yu, H. Ge, J.-Q. Wang, H.-F. Wang, K.-F. Liu, T. Wu, C. He, M.-H. Lu, Y.-F. Chen, Topological surface acoustic waves. *Phys. Rev. Appl.* **16**, 044008 (2021).
45. W. Cheng, E. Prodan, C. Prodan, Experimental demonstration of dynamic topological pumping across incommensurate bilayered acoustic metamaterials. *Phys. Rev. Lett.* **125**, 224301 (2020).
46. M. H. Holmes, *Introduction to Perturbation Methods*, (Springer Science & Business Media, 2012), vol. 20.

**Acknowledgments**

**Funding:** This work is supported by the Air Force Office of Scientific Research under grant no. AF 9550-18-1-0342 and AF 9550-20-1-0279 with Program Manager B.-L. (Les) Lee, the Army Research Office under grant no. W911NF-18-1-0031 with Program Manager D. P. Cole, the Army Research Office under grant no. W911NF-18-1-0031 with Program Manager D. P. Cole, and the NSF CMMI under award no. 1930873. R.Z. acknowledges support from the National Natural Science Foundation of China (NSFC) under grant no. 11991033. E.P. acknowledges support from the NSF through the grants DMR-1823800 and CMMI-2131760. **Author contributions:** Conceptualization: S.W., Q.W., H.C., and G.H. Methodology: S.W., Z.H., Q.W., R.Z., and G.H. Investigation: S.W., Z.H., R.Z., and G.H. Visualization: S.W. and Z.H. Funding acquisition: E.P., R.Z., and G.H. Writing (original draft): S.W., Z.H., Q.W., H.C., E.P., R.Z., and G.H. **Competing interests:** The authors declare that they have no competing interests. **Data and materials availability:** All data needed to evaluate the conclusions in the paper are present in the paper and/or the Supplementary Materials.

Submitted 3 March 2023

Accepted 26 June 2023

Published 28 July 2023

10.1126/sciadv.adh4310

# Science Advances

## Smart patterning for topological pumping of elastic surface waves

Shaoyun Wang, Zhou Hu, Qian Wu, Hui Chen, Emil Prodan, Rui Zhu, and Guoliang Huang

*Sci. Adv.*, **9** (30), eadh4310.  
DOI: 10.1126/sciadv.adh4310

### View the article online

<https://www.science.org/doi/10.1126/sciadv.adh4310>

### Permissions

<https://www.science.org/help/reprints-and-permissions>

Supplementary Materials for  
**Smart patterning for topological pumping of elastic surface waves**

Shaoyun Wang *et al.*

Corresponding author: Rui Zhu, ruizhu@bit.edu.cn; Guoliang Huang, huanggg@missouri.edu

*Sci. Adv.* **9**, eadh4310 (2023)  
DOI: 10.1126/sciadv.adh4310

**The PDF file includes:**

Supplementary Text  
Figs. S1 to S9  
Table S1  
Legend for movie S1

**Other Supplementary Material for this manuscript includes the following:**

Movie S1

# Supplementary Materials

## 1. Parameters, mode shape and fabrication

The geometric parameters for the topological pumping system are shown in Fig. S1, whereas the values of geometric and material parameters are shown in Table 1. The mode shapes of the three branches surface dispersion curves of the unit cell are shown in Fig. S2.

## 2. Tight-binding approximation in elasticity

For the host media with pillar array, we use the number pair  $(m, n)$  to express the coordinates of pillars whose sizes are all same. The connecting thin plates along synthetic dimension  $z$ , or between  $(m, n)$  pillar and  $(m, n + 1)$  pillar, are same for all  $(m, n)$ . The length  $w_1$  and the width  $t_1$  for all thin plates between  $(m, n)$  and  $(m + 1, n)$  are same. The height  $h$  of thin plate between  $(m, n)$  and  $(m + 1, n)$  is modulated as  $h_{mn} = h_0 [1 + \Delta_0 \cos (2\pi m/3 + \phi_n)]$ . For the host media with a single pillar (see Fig. S3A), the displacement field is

$$\mathbf{u}(\vec{r}). \quad (\text{S1})$$

For the host media with pillar array, the  $\alpha$ -th mode function in the pillar with coordinates  $(m, n)$  is

$$\mathbf{u}^\alpha(\vec{r} - \vec{R}_{mn}), \quad (\text{S2})$$

where  $\vec{R}_{mn} = m\vec{a}_1 + n\vec{a}_3$ , where  $\vec{a}_1$  and  $\vec{a}_3$  are basis vectors along horizontal and vertical directions. Since only one mode is excited in our problem, we just consider that mode and drop the  $\alpha$  index directly. And for simplicity, we use  $\mathbf{u}_{mn}$  to represent the eigenmode

$$\mathbf{u}_{mn} = \mathbf{u}(\vec{r} - \vec{R}_{mn}). \quad (\text{S3})$$

Since the connecting plates are very small, the coupling between two near pillars is very small. Therefore, we can use tight-binding model assumption which states that displacement

field of the whole structure can be assumed as the superposition of the eigenmode of each single pillar (see Fig. S3B):

$$\mathbf{u} = \sum_{mn} \psi_{m,n} \mathbf{u}_{mn}, \quad (\text{S4})$$

where  $m$  and  $n$  go over all unit cells along direction  $x$  and  $z$ .

The governing equations for cuboid  $\Omega$ , the hosted media and the attached pillars, in elasticity are (47)

$$L\mathbf{u} = -\rho\tilde{\omega}^2\mathbf{u}. \quad (\text{S5})$$

where  $L$  is the differential operator for governing equations in elasticity. Timing  $\mathbf{u}_{ij}$  to the terms at both sides and then doing the integration over the cuboid  $\Omega$ , we have

$$\int_{\Omega} \mathbf{u}_{ij} L \mathbf{u} dV = -\rho\tilde{\omega}^2 \int_{\Omega} \mathbf{u}_{ij} \mathbf{u} dV. \quad (\text{S6})$$

Expanding Eq. (S6) by using the Eq. (S4) gives the linear equations for the coefficients of the eigenmodes:

$$\begin{aligned} & \int_{\Omega} \mathbf{u}_{ij} L \mathbf{u}_{ij} dV \psi_{i,j} + \int_{\Omega} \mathbf{u}_{ij} L \mathbf{u}_{i-1,j} dV \psi_{i,j} + \int_{\Omega} \mathbf{u}_{ij} L \mathbf{u}_{i+1,j} dV \psi_{i,j} + \\ & \int_{\Omega} \mathbf{u}_{ij} L \mathbf{u}_{i,j-1} dV \psi_{i,j-1} + \int_{\Omega} \mathbf{u}_{ij} L \mathbf{u}_{i,j+1} dV \psi_{i,j+1} = -M\tilde{\omega}^2 \psi_{ij}, \end{aligned} \quad (\text{S7})$$

where only nearest neighbor and self overlapping integral are considered due to the tight-binding assumption. Now we define the overlapping integrals as the stiffness constants:

$$\kappa^g = \int_{\Omega} \mathbf{u}_{ij} L \mathbf{u}_{ij} dV, \quad \kappa_{ij}^h = \int_{\Omega} \mathbf{u}_{ij} L \mathbf{u}_{i+1,j} dV, \quad \text{and } \kappa^v = \int_{\Omega} \mathbf{u}_{ij} L \mathbf{u}_{i,j+1} dV. \quad (\text{S8})$$

In addition, we preset the modulations of  $h_{mn}$  is very weak, in other words  $\Delta_0 \rightarrow 0$ , so we can use the Taylor's expansion of the stiffness function:

$$\kappa_{ij}^h \approx \kappa^h(h_0) + h_0 \Delta_0 \cos(2\pi i/3 + \phi_j) \left. \frac{d\kappa^h}{dh} \right|_{h=h_0} = \kappa_0 [1 + \Delta \cos(2\pi i/3 + \phi_j)] \quad (\text{S9})$$

which indicates that  $\kappa_{ij}^h$  is topologically modulated (30). By defining  $\kappa^0 = \kappa^g + 2\kappa^v$ , we can rewrite Eq. (S7) as

$$\kappa^0 \psi_{i,j} + \kappa_{i-1,j}^h \psi_{i-1,j} + \kappa_{i,j}^h \psi_{i+1,j} + \kappa^v [\psi_{i,j-1} - 2\psi_{i,j} + \psi_{i,j+1}] = -M\tilde{\omega}^2 \psi_{i,j}. \quad (\text{S10})$$

which is the governing equations for the discrete model in Fig. S3C. To rewrite Eq. (S10) more compact, we define a column vector function

$$\boldsymbol{\psi}(z) = [\psi_0(z), \psi_1(z), \dots, \psi_{3M}(z)]^T, \quad (\text{S11})$$

where  $\psi_{i,j} = \psi_i(z)$  with  $z = ja$ , and a stiffness matrix whose elements are

$$K_{ik}(z) = [\kappa^0 \delta_{ik} + \kappa_i^h(z) \delta_{i,k+1} + \kappa_i^h(z) \delta_{i+1,k}] / \kappa^v. \quad (\text{S12})$$

And we define the first-order central difference formula

$$\delta f(z) = \frac{f(z + \frac{a}{2}) - f(z - \frac{a}{2})}{a}, \quad (\text{S13})$$

and the second-order central difference formula

$$\delta^2 f(z) = \frac{f(z + a) - 2f(z) + f(z - a)}{a^2}. \quad (\text{S14})$$

With Eq. (S11-S14), we can rewrite Eq. (S10) to

$$a^2 \delta^2 \boldsymbol{\psi}(z) + [\mathbf{K}(z) + \omega^2 \mathbf{I}] \boldsymbol{\psi}(z) = 0 \quad (\text{S15})$$

where  $M$  is set as 1, and we define a normalized  $\omega$  as  $\omega^2 = \tilde{\omega}^2 / \kappa^v$ . Finally, we get a matrix equation from the initial partial differential equation by using tight-binding model approximation. As long as the connecting pillars are not very large, the couplings between central pillars are not very large, and the tight binding approximation is reliable. Therefore, we can use such a simple matrix equation to obtain all desired information such as the wave propagation and topology of the system instead of solving the very complex partial differential equations in elasticity directly. Besides, Eq. (S15) has an analytical solution under adiabatic conditions, and it gives us lots of intuition to understand and design the system.

### 3. A WKB-type analysis

If  $\mathbf{K}(z)$  is a slowly-varying function, in other words,  $a \rightarrow 0$ , it looks like the standard equation for using the WKB method (21, 46, 48, 49). However, our equation is a difference matrix equation, we use the following asymptotic expansion of the solution

$$\psi(z) = e^{i\theta(z)/a} [\psi^{(0)}(z) + a\psi^{(1)}(z) + \dots], \quad (\text{S16})$$

where  $\psi^{(0)}(z)$  and  $\psi^{(1)}(z)$  are vectors. At first, we derive the following relation

$$\delta e^{i\theta(z)/a} = \frac{e^{i\theta(z+a/2)/a} - e^{i\theta(z-a/2)/a}}{a} = 2ia^{-1} \sin\left(\frac{\delta\theta}{2}\right) e^{i\theta(z)/a}. \quad (\text{S17})$$

Therefore, we get

$$\delta\psi(z) = \left[ 2ia^{-1} \sin\left(\frac{\delta\theta}{2}\right) \psi^{(0)} + 2i \sin\left(\frac{\delta\theta}{2}\right) \psi^{(1)} + \delta\psi^{(0)} \right] e^{i\theta(z)/a}, \quad (\text{S18})$$

and

$$\begin{aligned} \delta^2\psi(z) &= \left[ -a^{-2}4 \sin^2\left(\frac{\delta\theta}{2}\right) \psi^{(0)} - a^{-1}4 \sin^2\left(\frac{\delta\theta}{2}\right) \psi^{(1)} \right. \\ &\quad \left. + a^{-1}4i \sin\left(\frac{\delta\theta}{2}\right) \delta\psi^{(0)} + a^{-1}2i\delta \sin\left(\frac{\delta\theta}{2}\right) \psi^{(0)} \right] e^{i\theta(z)/a}, \end{aligned} \quad (\text{S19})$$

With the substitution of Eq. (S19) into Eq. (S15), we have

$$\begin{aligned} &-4 \sin^2\left(\frac{\delta\theta}{2}\right) \psi^{(0)} - 4a \sin^2\left(\frac{\delta\theta}{2}\right) \psi^{(1)} + 4ai \sin\left(\frac{\delta\theta}{2}\right) \delta\psi^{(0)} \\ &+ 4ai\delta \sin\left(\frac{\delta\theta}{2}\right) \psi^{(0)} + [\mathbf{K}(z) + \omega^2 \mathbf{I}] [\psi^{(0)}(z) + a\psi^{(1)}(z)] = 0, \end{aligned} \quad (\text{S20})$$

where up to the first order of  $a$  is kept. The leading order term gives

$$(\mathbf{K}(z) + \omega^2 \mathbf{I}) \psi^{(0)}(z) = 4 \sin^2\left(\frac{\delta\theta}{2}\right) \psi^{(0)}(z) \quad (\text{S21})$$

For  $\mathbf{K}(z)$ , we can define the corresponding instantaneous eigenvalue  $\mu_n(z)$  and eigenvector  $\varphi_n(z)$  from the eigenvalue problem

$$\mathbf{K}(z) \varphi_n(z) = -\mu_n(z) \varphi_n(z), \quad (\text{S22})$$

which is physically corresponding to an isolated chain without springs along synthetic dimension  $z$ . Substituting Eq. (S22) into Eq. (S21), we have the relation

$$2 \sin \left( \frac{\delta\theta_n}{2} \right) = \pm \sqrt{\omega^2 - \mu_n(z)}, \quad (\text{S23})$$

or

$$\delta\theta_n = 2 \arcsin \left( \frac{\pm \sqrt{\omega^2 - \mu_n(z)}}{2} \right) \quad (\text{S24})$$

and

$$\theta_n(z) = \theta_0 + a \sum_{\xi=0}^{\xi=z} 2 \arcsin \left( \frac{\pm \sqrt{\omega^2 - \mu_n(\xi)}}{2} \right) \quad (\text{S25})$$

If the eigenvalues are not degenerate, Eq. (S22) defines a set of complete and orthonormal basis functions. We can use them to construct the general solution of Eq. (1) by using the superposition of these basis functions

$$\psi(z) = \sum_l c_l(z) e^{i\theta_l(z)/a} \varphi_l(z) + a \sum_{lm} d_{lm}(z) e^{i\theta_l(z)/a} \varphi_m(z) + \dots, \quad (\text{S26})$$

Similarly, substituting Eq. (S26) into Eq. (S15), we have

$$\begin{aligned} & a \sum_l \left[ 4i\delta c_l \sin \left( \frac{\delta\theta_l}{2} \right) + 2ic_l \delta \sin \left( \frac{\delta\theta_l}{2} \right) \right] \varphi_l e^{i\theta_l/a} \\ & + \sum_{lm} \left[ -4 \sin^2 \left( \frac{\delta\theta_m}{2} \right) + \omega^2 - \mu_m \right] d_{lm} \varphi_m e^{i\theta_l/a} = 0, \end{aligned} \quad (\text{S27})$$

where the terms of  $a^n$  where  $n > 1$  are neglected, and  $\delta\varphi_l = \delta^2\varphi_l = 0$  are used due to eigenvectors are real and orthonormal. Besides, the second term on the left-hand side is equal to 0 due to Eq. (S23). Finally, timing  $\varphi_r$  on the left side and using the orthonormal relation, we have

$$4i\delta c_l \sin \left( \frac{\delta\theta_l}{2} \right) + 2ic_l \delta \sin \left( \frac{\delta\theta_l}{2} \right) = 0, \quad (\text{S28})$$

or

$$\delta c_l = -\frac{\delta \sin \left( \frac{\delta\theta_l}{2} \right)}{2 \sin \left( \frac{\delta\theta_l}{2} \right)} c_l. \quad (\text{S29})$$

The solution is

$$c_l(z) = \frac{c_1}{\sqrt{\sin\left(\frac{\delta\theta_l}{2}\right)}}. \quad (\text{S30})$$

Substituting Eq. (S23) into the solution of Eq. (S30), we have

$$c_l(z) = \frac{c_1}{\sqrt[4]{\omega^2 - \mu_l(z)}}. \quad (\text{S31})$$

Finally, we have one special solution of the  $l$ th eigenstate

$$\psi_l(z) = \frac{c_1}{\sqrt[4]{\omega^2 - \mu_l(z)}} e^{i \sum_{\xi=0}^{\xi=z} 2 \arcsin\left(\frac{\sqrt{\omega^2 - \mu_l(\xi)}}{2}\right)} \varphi_l(z) \quad (\text{S32})$$

Since the difference equation is in second-order, there are two linear independent special solutions. The other special solution can be obtained by take the conjugation of the first special solution easily, so we can have the general solution by the superposition of two special solutions

$$\begin{aligned} \psi_l(z) &= \frac{c_1}{\sqrt[4]{\omega^2 - \mu_l(z)}} e^{i \sum_{\xi=0}^{\xi=z} 2 \arcsin\left(\frac{\sqrt{\omega^2 - \mu_l(\xi)}}{2}\right)} \varphi_l(z) \\ &\quad + \frac{c_2}{\sqrt[4]{\omega^2 - \mu_l(z)}} e^{-i \sum_{\xi=0}^{\xi=z} 2 \arcsin\left(\frac{\sqrt{\omega^2 - \mu_l(\xi)}}{2}\right)} \varphi_l(z). \end{aligned} \quad (\text{S33})$$

where  $c_1$  and  $c_2$  are two superposition coefficients. In addition, we can introduce a instantaneous wave number

$$q_l(z) = 2 \arcsin\left(\frac{\sqrt{\omega^2 - \mu_l(z)}}{2}\right), \quad (\text{S34})$$

and Eq. (S33) can be reduced as

$$\psi_n(z) = \frac{c_1}{\sqrt[4]{\omega^2 - \mu_n(z)}} e^{i \sum_z q_n(z)} \varphi_n(z) + \frac{c_2}{\sqrt[4]{\omega^2 - \mu_n(z)}} e^{-i \sum_z q_n(z)} \varphi_n(z), \quad (\text{S35})$$

where index  $l$  is changed to index  $n$ .

From Eq. (S35), we found the wave field for  $z$ th row is the corresponding eigenmode  $\varphi_n(z)$  for the isolated chain with the multiplication of a phase factor  $e^{-i \sum_z q_n(z)}$  and an amplitude

$\frac{c}{\sqrt[4]{\omega^2 - \mu_n(z)}}$ . It actually gives the adiabatic theorem that the system will keep staying on the  $n$ th eigenstate if the system stays in  $n$ th eigenstate initially (50). Moreover, the analytical expression of phase factor can give the instruction to phase engineering with topological pumping.

To derive Eq. (S35), we only impose the adiabatic condition, and we didn't use long wave approximation and paraxial approximation, which are commonly used to reduce the second-difference equation to a first-order differential equation (Schrödinger's equation) since it has the adiabatic solution (50). Once these approximations are used, these theories fail for short wave length region and nonparaxial region (35, 51). Nevertheless, our solution Eq. (S35) suits for large wave number up to the irreducible Brillouin zone boundaries and nonparaxial region, and it can be reduced to these theories by just taking  $q_n(z) \rightarrow 0$ .

Considering the long wave approximation  $q_n(z) \rightarrow 0$ , we can substitute the discrete summation by the continuous integral:

$$\psi_n(z) = \frac{c_1}{\sqrt[4]{q_n(z)}} e^{i \int_z q_n(z) dz} \varphi_n(z) + \frac{c_2}{\sqrt[4]{q_n(z)}} e^{-i \int_z q_n(z) dz} \varphi_l(z). \quad (\text{S36})$$

And Eq. (S34) can be reduced as

$$4 \sin^2 \frac{q_n(z)}{2} + \mu_n(z) = \omega^2. \quad (\text{S37})$$

One of the special solution in Eq. (S36) and frequency intersection equation (Eq. (S37)) are same as the results in reference (35) where paraxial approximation and long wave approximation are used.

To excite the wave, we should choose the frequency  $\omega$  as the excitation frequency  $\omega_c$ , and  $\mu_n(z)$  can be obtained by solving the eigenvalue problem Eq. (S22) which is physically corresponding to an isolated chain without springs along  $z$  direction, and the instantaneous wave number  $q_n(z)$  can be obtained by solving Eq. (S37) geometrically. Alternatively, we can collect the two terms on the left-hand side in Eq. (S37) together as the eigenvalue problem of a chain

with springs  $\kappa^z$  along synthetic dimension  $z$  and with imposing Floquet periodic boundary of wave number  $k_z$ , which is actually the conditions used for supercell in finite element simulation.

## 4. Eigenmode and spectrum

In previous section, we give the solution in Eq. (S33), which is a wave propagating in infinite media physically. Now we turn to discuss the vibration problem with imposing boundary conditions. The general solution is

$$\psi(z) = \sum_n \frac{\varphi_n(z)}{\sqrt[4]{\omega^2 - \mu_n(z)}} \left[ c_n \sin \sum_z q_n(z) + d_n \cos \sum_z q_n(z) \right] \quad (\text{S38})$$

The boundary conditions of the lattice system along vertical direction are

$$\begin{aligned} \Delta\psi(0) + [\omega^2 \mathbf{I} - \mathbf{K}(z)]\psi(0) &= 0 \\ -\Delta\psi(L) + [\omega^2 \mathbf{I} - \mathbf{K}(z)]\psi(L) &= 0, \end{aligned} \quad (\text{S39})$$

where  $\Delta f(z) = [f(z+a) - f(z)]/a$ . Substitution of Eq. (S38) into  $\Delta\psi(z) + [\omega^2 \mathbf{I} - \mathbf{K}(z)]\psi(z) = 0$  gives

$$\begin{aligned} \sum_n \left[ \frac{\Delta\varphi_n(z)}{\sqrt[4]{\omega^2 - \mu_n(z)}} + \varphi_n(z) \Delta \left( \frac{1}{\sqrt[4]{\omega^2 - \mu_n(z)}} \right) \right] \left[ c_n \sin \sum_z q_n(z) + d_n \cos \sum_z q_n(z) \right] \\ + \sum_n \frac{\varphi_n(z)}{\sqrt[4]{\omega^2 - \mu_n(z)}} \left[ c_n q_n(z) \cos \sum_z q_n(z) - d_n q_n(z) \sin \sum_z q_n(z) \right] \\ + \sum_n \frac{[\omega^2 - \mu_n(0)] \varphi_n(z)}{\sqrt[4]{\omega^2 - \mu_n(z)}} \left[ c_n \sin \sum_z q_n(z) + d_n \cos \sum_z q_n(z) \right] = 0 \end{aligned} \quad (\text{S40})$$

After timing  $\varphi_n^\dagger(z)$  on the left side, we have

$$\begin{aligned} c_n [q_n(z) \cos q_n(z) + (\omega^2 - \mu_n(z)) \sin q_n(z)] \\ + d_n [-q_n(z) \sin q_n(z) + (\omega^2 - \mu_n(z)) \cos q_n(z)] = 0 \end{aligned} \quad (\text{S41})$$

where orthogonality and normalization of  $\varphi_n(z)$ , or  $\Delta\varphi_n(z) = 0$ , and slowly-varying assumption, or  $\Delta \left( \frac{1}{\sqrt[4]{\omega^2 - \mu_n(z)}} \right) = 0$ , are used. By substituting  $z$  to 0 and  $L$  in Eq. (S41), we have

$$\begin{aligned} & c_n [q_n(o) \cos q_n(0) + (\omega^2 - \mu_n(0)) \sin q_n(0)] \\ & + d_n [-q_n(0) \sin q_n(0) + (\omega^2 - \mu_n(0)) \cos q_n(0)] = 0, \\ & c_n [-q_n(L) \cos q_n(L) + (\omega^2 - \mu_n(L)) \sin q_n(L)] \\ & + d_n [q_n(L) \sin q_n(L) + (\omega^2 - \mu_n(L)) \cos q_n(L)] = 0, \end{aligned} \quad (\text{S42})$$

Vanishing the determinant of the the Eq. (S42) gives frequency spectrum

$$\begin{vmatrix} q_n(0) \cos q_n(0) + (\omega^2 - \mu_n(0)) \sin q_n(0) & -q_n(0) \sin q_n(0) + (\omega^2 - \mu_n(0)) \cos q_n(0) \\ -q_n(L) \cos q_n(L) + (\omega^2 - \mu_n(L)) \sin q_n(L) & q_n(L) \sin q_n(L) + (\omega^2 - \mu_n(L)) \cos q_n(L) \end{vmatrix} = 0. \quad (\text{S43})$$

Therefore, we have the eigenmode

$$\psi_n(z) = \frac{\varphi_n(z)}{\sqrt[4]{\omega_n^2 - \mu_n(z)}} \left[ c_n \sin \sum_z q_n(z) + d_n \cos \sum_z q_n(z) \right] \quad (\text{S44})$$

where eigenfrequency  $\omega_n$  is from Eq. (S43). In this paper, we don't compare Eq. (S44) with numerical or experimental mode profile directly, but verify the instantaneous wave number  $q_n z$  by using wavelet transform along vertical direction and instantaneous eigenmode  $\varphi_n(z)$  by doing mode decomposition.

## 5. Excitation

From the solution obtained from WKB approximation, we find that the system will keep in the eigenstate if the initial state is a eigenstate. Therefore, to excite the wave, we attach piezoelectric patches on the sides of first row pillars. Since we want to excite the  $n$ th order wave (Eq. (S32)), the voltages vector should be proportional to the eigenmode  $\varphi(0)$  and is defined as

$$\mathbf{V}(t) = V_0 \varphi_n(0) f_z(t). \quad (\text{S45})$$

where  $V_0 = 1$  V denotes the voltage amplitude, and  $f_z(t)$  is a 50-cycle tone burst signal  $f_z(t) = H(50/f_c - t)[1 - \cos(2\pi f_c t / 50)] \sin(2\pi f_c t)$  (top panel of Fig. 3), with  $H(t)$  being the Heaviside function and  $f_c = 41.88$  kHz. By using this excitation, we can excite the first chain with  $\varphi_n(0)$ , and then this mode will transport from the first chain to the final chain with keeping staying the eigenmode  $\varphi_n(z)$ .

To excite the eigenmode of the cuboid, we use the Green's function for point load  $\delta(\vec{r} - \vec{\xi})e^{i\omega t}$

(52)

$$g(\vec{r}, t | \vec{\xi}) = \sum_{n=1}^{\infty} c_n \psi_n(\vec{\xi}) \psi_n(\vec{r}) \frac{e^{i\omega t}}{\omega^2 - \omega_n^2} \quad (\text{S46})$$

where  $\psi$  is the  $n$ th eigenmode of cuboid,  $c_n$  is a coefficient,  $\vec{\xi}$  point load position,  $\omega_n$  is the  $n$ th eigenfrequency of cuboid. According to Eq. (S46), we just need to attach a piezoelectric patch on the side of cuboid (anywhere since excitation is not related to excitation position) by applying harmonic voltage as long as the excitation frequency is same as the eigenfrequency for the eigenmode we want to excite. To recognize different eigenmodes, we use the white noise excitation which includes all frequency components so all the eigenmodes are excited. But eigenmode can be recognized by doing Fourier transform of time signal of each point to frequency domain. In frequency domain, we check the modeshape for each resonating peak and we can find the EBE mode in our study.

## 6. Chern number

We consider the unit cell of Eq. (S15) by imposing periodic boundary conditions along  $x$  while the stiffness is modulated by the parameter  $\phi$ . The system follows Newton's equation in the frequency domain

$$\mathbf{D}(\phi, q)\psi = -\omega^2 \mathbf{I}\psi \quad (\text{S47})$$

where the dynamical matrix  $\mathbf{D}$  is

$$\mathbf{D}(\phi, q) = \begin{bmatrix} \kappa^0 & \kappa_1^h(\phi) & \kappa_3^h(\phi)e^{-iqx} \\ \kappa_1^h(\phi) & \kappa^0 & \kappa_2^h(\phi_x) \\ \kappa_3^h(\phi)e^{iqx} & \kappa_2^h(\phi) & \kappa^0 \end{bmatrix} \quad (\text{S48})$$

where  $\kappa_i^h(\phi) = \kappa_0 [1 + \Delta \cos(2i\pi/3 + \phi)]$  and  $\phi \in (0, 2\pi)$ .

This topological invariant is the Chern number, and we can calculate it by the integral of the Berry curvature on the Brillouin zone (BZ):

$$C_1 = \sum_{f_\beta < f_{\text{gap}}} \frac{1}{2\pi i} \int_{\text{BZ}} B_{lm}^\beta(\mathbf{k}) d^2\mathbf{k} \quad (\text{S49})$$

where the Berry curvature is

$$B_{lm}^\beta(\mathbf{k}) = \partial_{k_l} A_m^\beta(\mathbf{k}) - \partial_{k_m} A_l^\beta(\mathbf{k}), \quad (\text{S50})$$

where  $A_l^\beta = \langle \psi^\beta(\mathbf{k}) | \partial_l | \psi^\beta(\mathbf{k}) \rangle$  is the Berry connection. The two Chern number are  $-1$  and  $1$ , respectively.

## 7. Displacement selection of experimental measurement

The pillar resonators in the system primarily deform along the  $z$ -direction (see Fig. S4A), making it preferable to measure the vibration in that direction. However, it was not experimentally feasible to directly measure the  $z$ -directional velocity fields of all pillars using the 1D scanning laser Doppler vibrometer (Polytec PSV-500) because of the position blocking caused by surrounding pillars. To address this issue, we measured the  $y$ -directional velocity field at the top surface instead. Although its intensity was relatively small compared with the  $z$ -direction, measuring the  $y$ -component is still reasonable because the  $y$ -component along the edge can be proved to be linearly proportional to the  $z$ -component under the first eigenmode deformation. This relation is derived in detail below, according to the Euler-Bernoulli beam theory. For a cantilever beam with a finite length  $l$  shown in Fig. S4B, the  $z$ -directional deflection across the

beam under the fundamental deformation can be expressed as (53)

$$w(y) = A[(\sin \beta l + \sinh \beta l)(\cos \beta y - \cosh \beta y) - (\cos \beta l + \cosh \beta l)(\sin \beta y - \sinh \beta y)], \quad (\text{S51})$$

where  $w$  is transverse displacement,  $\beta$  is the wave number,  $A$  is the amplitude, and the slope of the deflection curve is

$$w'(y) = A(\beta \sin \beta y + \beta \sinh \beta y)(\sin \beta l + \sinh \beta l) + A(\beta \cos \beta y - \beta \cosh \beta y)(\cos \beta l + \cosh \beta l). \quad (\text{S52})$$

Based on Eqs. (S51-S52), the  $z$ -directional deflection, the slope, and the magnitude of  $y$ -directional displacement at the edge of the beam ( $y = l, z = \frac{t_0}{2}$ ) are

$$\begin{aligned} \delta_z &= A(2 \cosh \beta l \sin \beta l - 2 \cos \beta l \sinh \beta l), \\ w'(l) &= \tan \theta = 2A\beta \sin \beta l \sinh \beta l, \\ \delta_y &= z \tan \theta = At_0\beta \sin \beta l \sinh \beta l. \end{aligned} \quad (\text{S53})$$

And the ratio of  $\delta_y$  and  $\delta_z$  is

$$\frac{\delta_y}{\delta_z} = \frac{t_0\beta \sin \beta l \sinh \beta l}{2 \cosh \beta l \sin \beta l - 2 \cos \beta l \sinh \beta l}. \quad (\text{S54})$$

Under the first eigenmode with  $\beta l = 1.8751$  (53),  $l = a = 0.01$  m, and  $t_0 = 0.0035$  m, the linear relation of  $\delta_y$  and  $\delta_z$  is proved to be  $\delta_y = 0.24\delta_z$ .

To ensure maximum measurement accuracy and consistency of  $y$ -directional displacements across different pillars, we carefully selected the middle points ( $x = \frac{(2i-1)a}{2}, y = a, z = \frac{t_0}{2} + ja - \epsilon$ ) where  $i = 1, 2, \dots, 9, j = 1, 2, \dots, 20$  are pillar indices,  $\epsilon$  is the radius of laser spot and it is usually equal to 0.25 mm ) along one positive edge of the top surface of each pillar as the measurement points, as illustrated in Fig. S4C. This approach also helps to eliminate any possible displacement error resulting from the slightly twisted deformation of the pillar caused by the asymmetric geometries of the connection plates along the x-direction, since twisted deformation does not have a  $y$ -directional component.

## 8. Frequency spectra analysis of experimental measurement

Due to the presence of disorders, defects, and material parameter errors in real samples, the eigenfrequencies derived from experiments and simulations may not be exactly the same. To accurately determine the topological eigenmode frequency in the experiment, an analysis of the frequency spectra of the experimental measurement was carried out at specific corner points located at the end of the desired pumping path. These corner points are (1, 18), (2, 18), (1, 19), and (2, 19) and are shown in Fig. S5. Upon examining Fig. S5 near the simulated eigenfrequency 41.88kHz, several peaks were observed. After the check of the corresponding modal profile for each peak, the identification of the experimental eigenfrequency of the EBE mode was found to be 42.45kHz.

## 9. Design of topological pumping paths

By tuning the phason trajectories in the phason space, we can achieve different topological pumping paths. To showcase the tunability, we show four different paths in Fig. S6. The first illustration in Fig. S6A is a pump from the bottom right to the top left by configuring  $\phi(z) = 0.6\pi + 0.8\pi z/L$ . The second case shown in Fig. S6B is the opposite of the first case with  $\phi(z) = -0.4\pi + 0.8\pi z/L$ . The third case features a pump from the bottom right to the bulk with  $\phi(z) = 0.6\pi + 0.4\pi z/L$ , see Fig. S6C. The last illustration (Fig. S6D) is simply a combination of the first and second scenarios with  $\phi(z) = 0.6\pi + 0.4\pi z/L, z \in (0, L/2)$  and  $\phi(z) = 1.4\pi + 0.4\pi(L/2 - z)/L, z \in (L/2, L)$ .

## 10. The influence of defects at various positions of the topological pumping

Here, we confirm that the topological transport for surface waves is immune to defects, regardless of their positions. To demonstrate this, we add two additional defects at the bottom left (Fig. S7A) and top left (Fig. S7C) corners, in addition to the central defect included in the

main text (Fig. S7B). It can be seen from Fig. S7 that the eigenmodes and eigenfrequencies with defects are very similar to those without defects. Therefore, the topological surface wave transmission remains robust regardless of the defect location.

## 11. The influence of viscous damping on the topological pumping

Here, we consider the viscous damping by introducing an isotropic loss factor  $\eta$  into materials properties as  $\lambda \rightarrow \lambda(1 + i\eta)$  and  $\mu \rightarrow \mu(1 + i\eta)$ . Accordingly, the stiffness matrix is modified as  $\mathbf{K}(z) \rightarrow \mathbf{K}(z)(1 + i\eta)$ , and  $\mu_n(z) \rightarrow \mu_n(z)(1 + i\eta)$ . As a result, Eq. (10) in the main text becomes

$$4 \sin^2 \frac{q_n(z)}{2} + \mu_n(z)(1 + i\eta) = \omega^2. \quad (\text{S55})$$

Since  $\eta$  is very small ( $\eta = 10^{-4}$  for aluminum (54)), we can solve the above equation perturbatively by assuming  $q_n(z) \rightarrow q_n(z) + \frac{i\eta\mu}{4\sin q_n(z)}$ . The inverse of the imaginary part is the attenuation wavelength equal to  $a\eta^{-1}$  approximately. It indicates that waves experience significant attenuation after propagating through the medium for a distance of  $10000a$ . However, since our system is only  $20a$  in length, the energy consumption can be considered negligible and ignored. This is further supported by the frequency response analysis conducted using FEA software COMSOL, where the modal profile of the damped system (as shown in Fig. S8A) is very similar to that of the undamped system (as shown in Fig. S8B) when the loss factor is introduced.

To determine the energy transmission efficiency in experiment, we perform mode decomposition of measured displacement field at the first and final rows. The coefficients of 7th eigenmode (the EBE mode) are then obtained as

$$\begin{aligned} c_7(z=0) &= \varphi_7^T(z=0)\psi(z=0), \\ c_7(z=L) &= \varphi_7^T(z=L)\psi(z=L). \end{aligned} \quad (\text{S56})$$

from which the transmission efficiency defined as  $T = \frac{c_7(z=0)}{c_7(z=L)}$  can be calculated as 97.5%. As a

result, the energy loss is determined as  $1 - 0.975^2 = 4.94\%$ , which is close to 0. Therefore, for our current system, the energy consumption of wave transport along the path can be disregarded. and the wave transport efficiency is close to 100% based on our numerical and experimental results.

## 12. The frequency range for the topological pumping

The topological pumping of surface waves in this work is not limited to a single frequency at 42.45 kHz. As illustrated in Fig. 1D, the range of frequencies for feasible topological wave pumping is around 1 kHz, as indicated by the frequency range covered by the magenta surface (which corresponds to the EBE mode). Therefore, it is possible to achieve topological pumping for surface acoustic waves at multiple frequencies such as 41.78 kHz, 42.67 kHz, and 42.88 kHz by using the configuration studied in this work, as demonstrated by the EBE modes presented in Figs. S9A-C, respectively. To achieve a broader range of frequencies for wave pumping, one may increase the  $z$ -directional stiffness of the substrate. By doing so, the magenta surface will cover a wider frequency range.

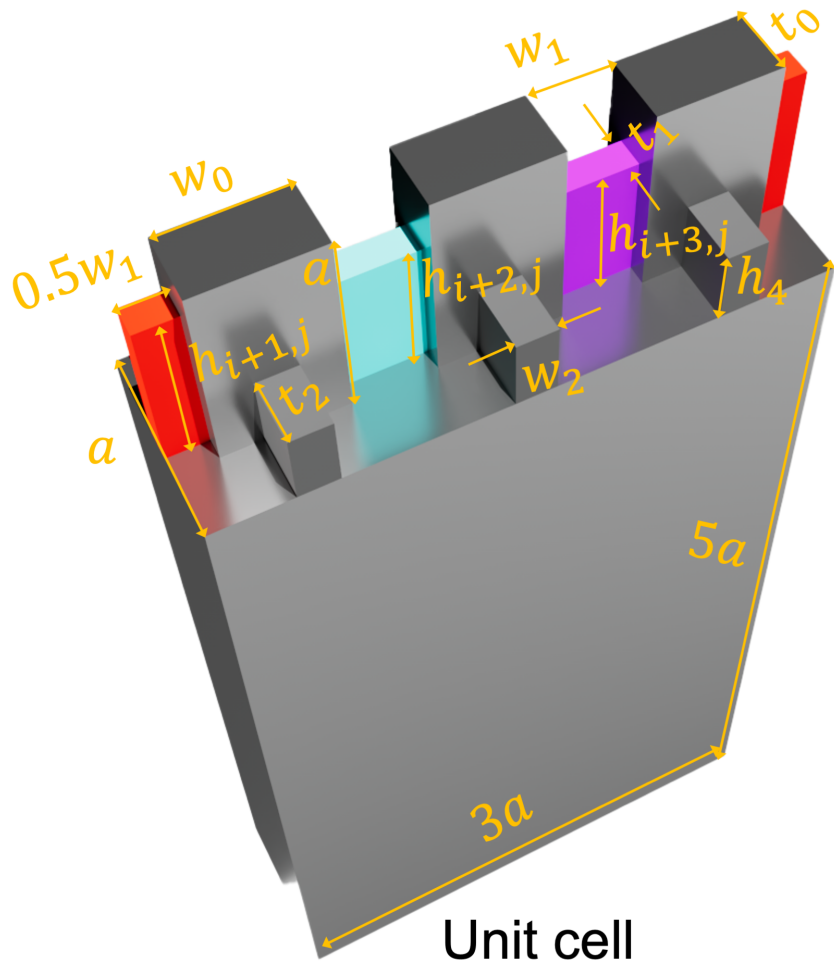


**Fig. S1.** The unit cell and the corresponding geometric parameters.

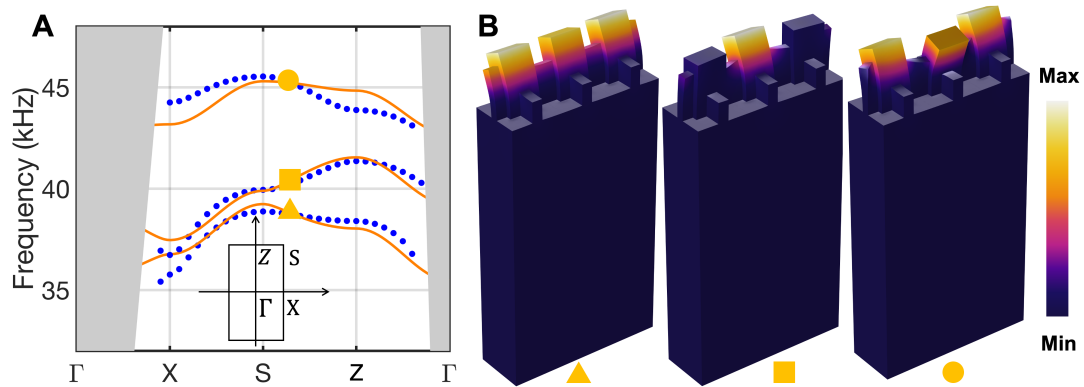


**Fig. S2. Dispersion curves on the Brillouin zone and its mode shapes.** (A) The dispersion curves (blue dots) of the unit cell on the boundaries of the irreducible Brillouin zone. (B) The representative mode shapes of 3 branches dispersion curves at triangle, square and circle position. The energy mainly locates on the surface, so they are surface modes.

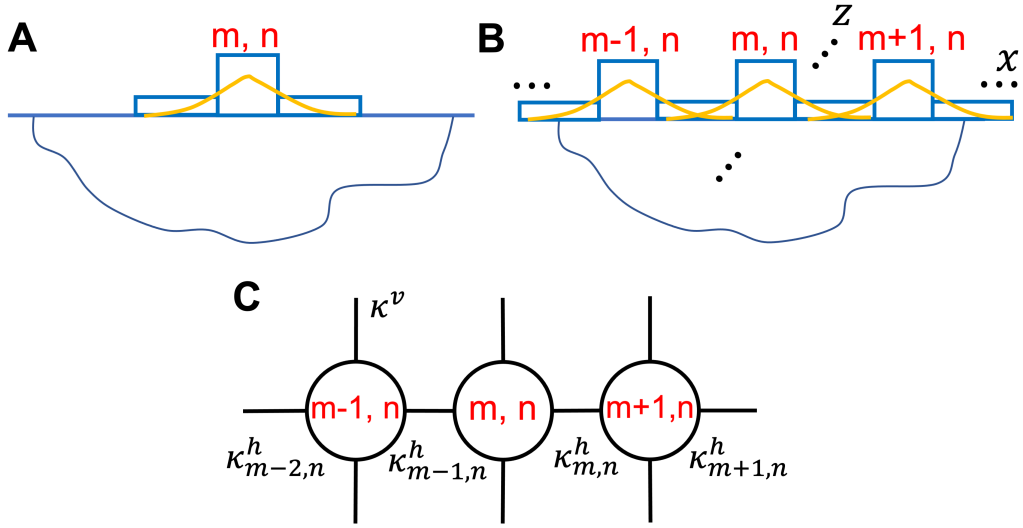


**Fig. S3. The schematic pictures of tight binding approximation.** (A). An isolated pillar and connections are attached on the surface whereas the displacement field is concentrated in the pillar (yellow line). (B). The pillar array and the connections. The overlap between two displacements field of two near isolated pillars is very small, so the total displacement field can be viewed as the superposition of all isolated pillar displacement field. (C). The effective discrete model of a unit cell from tight-binding approximation.

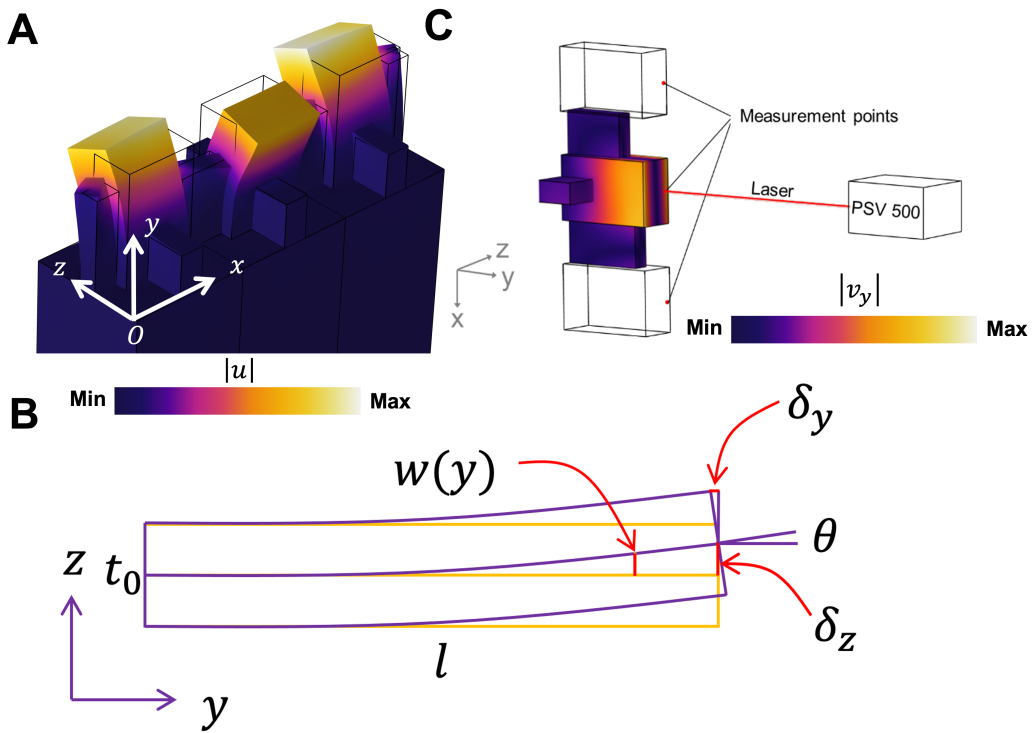


**Fig. S4. Bending analysis of pillar resonators in a unit cell.** (A) Bending towards the  $z$ -direction of pillar resonators in a unit cell. (B) The detail of bending deformation of a cantilever beam with thickness. (C) The measurement point is on the middle point of long side of top surface of each pillar, where the  $y$ -direction vibration velocity is measured by a 1D scanning laser Doppler vibrometer (PSV 500).

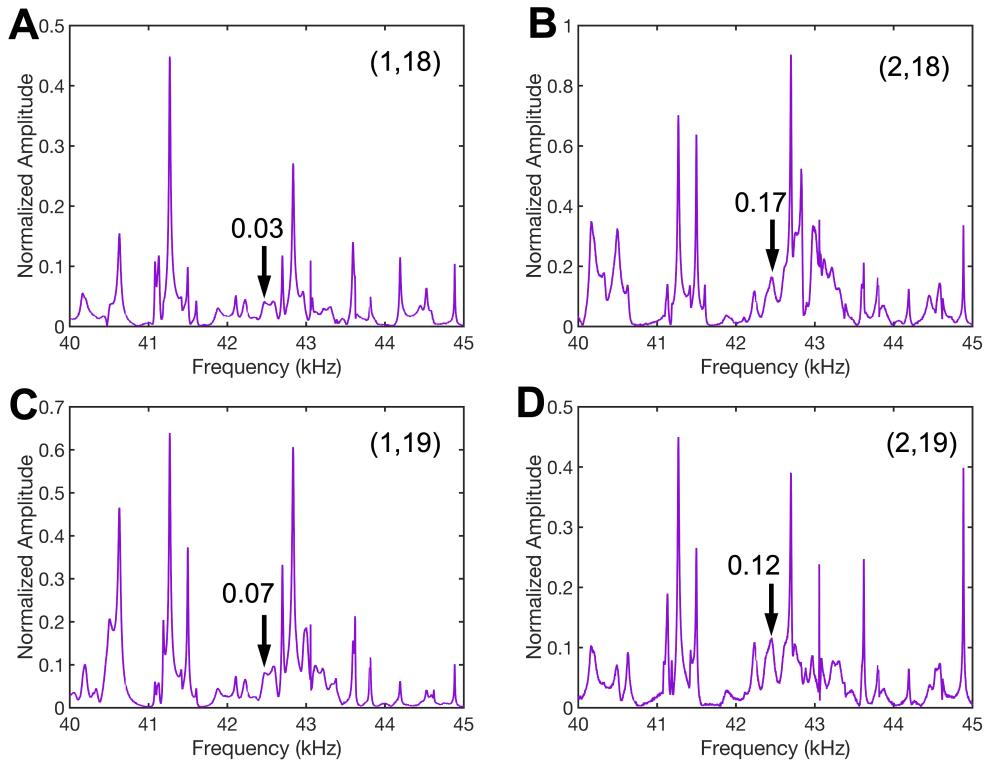


**Fig. S5. Frequency spectra at different positions.** The experimental frequency spectra at four different locations, namely (1,18), (2,18), (1,19), and (2,19), are shown in panels (A), (B), (C), and (D), respectively. The EBE modes are indicated by black arrows with their corresponding normalized amplitudes. All frequencies of EBE modes in 4 panels are 42.45 kHz.

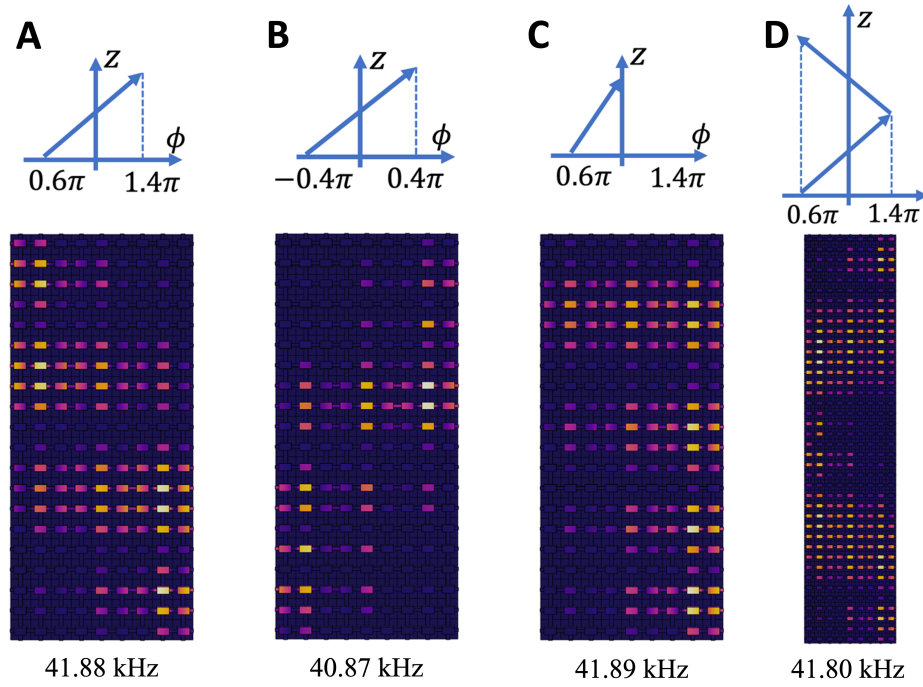


**Fig. S6. Design of multiple pumping paths by tuning phason trajectories.** **A)** Pumping from bottom right corner to top left corner whereas  $\phi = 0.6\pi + 0.8\pi z/L$ . **(B)** Pumping from bottom right corner to top left corner whereas  $\phi = -0.4\pi + 0.8\pi z/L$ . **(C)** Pumping from bottom left corner to the bulk whereas  $\phi = 0.6\pi + 0.4\pi z/L$ . **(D)** Pumping from bottom right corner to middle left and then to top right whereas  $\phi = 0.6\pi + 0.4\pi z/L, z \in (0, L/2)$  and  $\phi = 1.4\pi + 0.4\pi(L/2 - z)/L, z \in (L/2, L)$ .

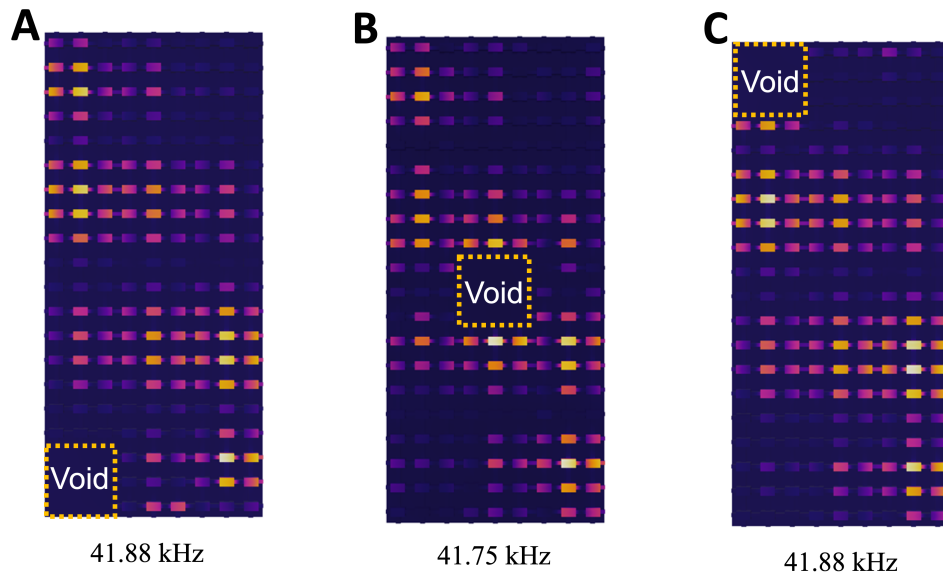


**Fig. S7. Influence of eigenmode and eigenfrequency by defects at different positions..** (A) Defect is located on the bottom left. (B) Defect is located at the center. (C) Defect is located on the top left.

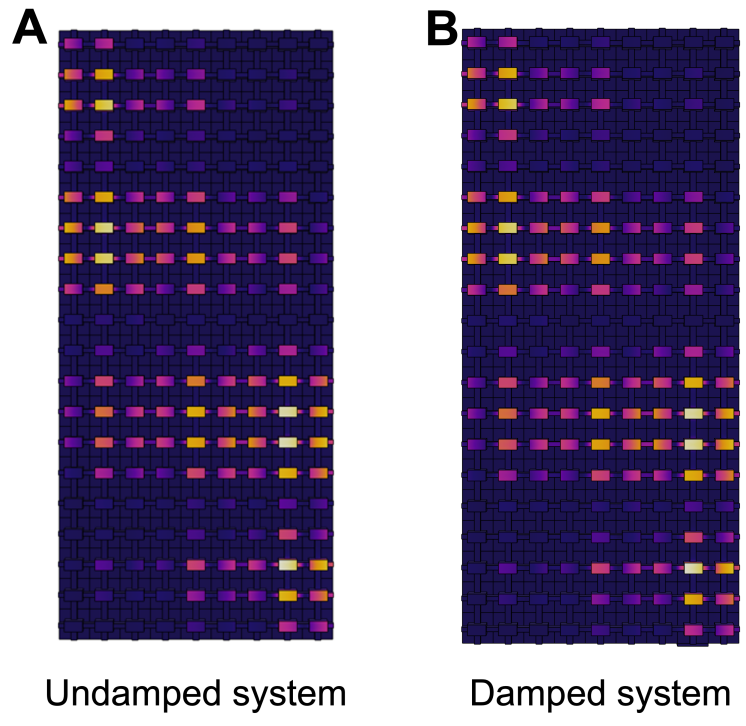


**Fig. S8. Influence of viscous damping on frequency response field.** (A) Frequency response at 41.88kHz in a damped system with  $\eta = 10^{-4}$ . (B) Frequency response at 41.88kHz in undamped system.

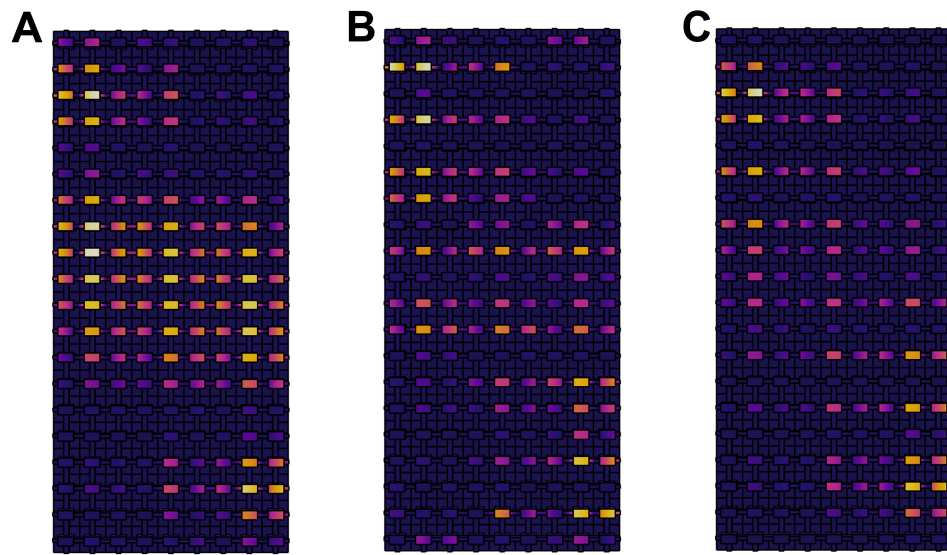


**Fig. S9. Eigenmodes at different frequencies in simulation.** (A), (B) and (C) Eigenmodes at frequencies 41.78 kHz, 42.67 kHz, and 42.88 kHz.

Table 1: Geometric and material parameters for the structure

Geometric parameters			
Parameter name	Value	Parameter name	Value
$a$	10 mm	$h_1$	$h_0 [1 + \delta \cos(2\pi/3 + \phi(z))]$
$w_0$	$0.6a$	$h_2$	$h_0 [1 + \delta \cos(4\pi/3 + \phi(z))]$
$w_1$	$0.4a$	$h_3$	$h_0 [1 + \delta \cos(6\pi/3 + \phi(z))]$
$w_2$	$0.2a$	$h_0$	$0.7a$
$t_0$	$0.35a$	$\Delta_0$	0.15
$t_1$	$0.15a$	$\phi(z)$	$\phi_s + (\phi_f - \phi_s)z/L_z$
$t_2$	$0.325a$	$\phi_s$	$0.6\pi$
$L_z$	$20a$	$\phi_f$	$1.4\pi$
$L_x$	$9a$		
Material parameters of Aluminum			
Parameter name	Value	Parameter name	Value
Young's module $E$	69 Gpa	Poisson's ratio $\nu$	0.33
Density $\rho$	2700 kg/m <sup>3</sup>		

**Movie S1.** The movie for transient analysis of the pumping process is shown in Fig. 3 in the main text.